ZNHIT1-dependent H2A.Z deposition at meiotic prophase I underlies pachytene gene expression and meiotic progression during male meiosis

Shenfei Sun[1,2,5,*], Yamei Jiang[2,5], Ning Jiang[2,5], Qiaoli Zhang[2], Hongjie Pan[3], Fujing Huang[2], Xinna Zhang[1], Yuxuan Guo[1], Xiaoyu You[2], Kai Gong[2], Wei Wei[2], Hanmin Liu[4], Zhenju Song[2], Yuanlin Song[2], Xiaofang Tang[2], Miao Yu[2], Runsheng Li[3], Xinhua Lin[1,2,4*]

Affiliations

[1]State Key Laboratory of Reproductive Regulation and Breeding of Grassland Livestock, Institutes of Biomedical Sciences, School of Life Sciences, Inner Mongolia University, Hohhot 010070, China;

[2]State Key Laboratory of Genetic Engineering, Greater Bay Area Institute of Precision Medicine (Guangzhou), School of Life Sciences, Zhongshan Hospital, Fudan University, Shanghai 200438, China;

[3]National Health Commission (NHC) Key Laboratory of Reproduction Regulation, Shanghai Institute for Biomedical and Pharmaceutical Technologies, Shanghai 200032, China;

[4]The Joint Laboratory for Lung Development and Related Diseases of West China Second University Hospital, Sichuan University and School of Life Sciences of Fudan University, Chengdu 610041, China;

[5]These authors contributed equally to this work.

[*]Correspondence to: xlin@fudan.edu.cn (X.L.); shenfei_sun@fudan.edu.cn (S.S.).

Keywords: male meiosis; pachytene gene expression; meiotic progression; ZNHIT1; H2A.Z

Abstract

Accurate meiotic progression is important for gamete formation and the generation of genetic diversity. However, little is known about the identity of chromatin regulators that underlie mammalian meiosis in vivo. Here, we identify the multifaceted functions of the chromatin remodeler ZNHIT1 in governing meiosis. The expression of *Znhit1* gradually increases during the meiotic prophase, and *Znhit1* knockout in spermatocytes results in arrested pachytene development, impaired DNA double-strand break repair, and defective homologous recombination. Single-cell RNA sequencing and transcriptome analysis reveal that *Znhit1* loss dysregulates meiotic transcriptional programs at the pachytene stage. Chromatin immunoprecipitation data show that ZNHIT1 is needed for the incorporation of the histone variant H2A.Z into pachytene chromatin. Moreover, we found that H2A.Z cooperates with the transcription factor A-MYB to co-bind DNA elements and control gene activity. Our findings provide insights into the regulatory mechanisms governing meiotic progression and highlight ZNHIT1 as a critical regulator of meiotic progression.

Introduction

Meiosis is a fundamental and conserved process that plays a crucial role in gamete formation and the generation of genetic diversity. By undergoing one round of DNA replication and two rounds of cell division, the meiotic process ensures the production of haploid cells, each with a unique combination of genetic materials (Handel and Schimenti, 2010; Lascarez-Lagunas et al., 2020). Any disruptions to the normal progression of meiosis would have significant consequences, such as aneuploidy, infertility, spontaneous abortion, and congenital diseases (Hassold and Hunt, 2001). Therefore, understanding the molecular mechanisms underlying meiosis will provide valuable insights for the diagnosis and treatment of reproductive and developmental diseases.

Multiple chromosomal events occur during meiotic prophase I, including homologous chromosome pairing and synapsis, DNA double-strand break (DSB) formation and repair, and homologous recombination (HR) (Baudat et al., 2013; Hunter, 2015; Zickler and Kleckner, 2023). In this process, homolog pairing and synapsis coincide with SPO11-mediated genome-wide formation of DSBs (Bergerat et al., 1997; Keeney et al., 1997). Following the formation of DSBs, the DNA undergoes resection, leading to the generation of single-stranded DNA overhangs. These overhangs are then coated by RPA, DMC1, and RAD51, facilitating the production of recombination intermediates. Subsequently, these intermediates are processed and resolved, ultimately forming either meiotic crossovers or non-crossovers (Gray and Cohen, 2016; San Filippo et al., 2008; Symington, 2014). The tightly coordinated timing and spatial arrangement of these meiotic events are of utmost importance for proper germ cell development.

There is transcriptional awakening during male meiotic prophase I, in which the meiotic genome becomes transcriptionally active during the zygotene-to-pachytene transition (Alexander et al., 2023; Ernst et al., 2019; Green et al., 2018; Rabbani et al., 2022; Turner, 2015). This process, referred to as pachytene genome activation (PGA) in this context, is responsible for the expression of numerous genes and plays an essential role in controlling meiotic and post-meiotic events. Previous studies have emphasized the significance of the transcription factors (TFs) A-MYB, BRDT, and TCFL5 in activating transcription during pachytene (Alexander et al., 2023; Bolcun-Filas et al., 2011; Cecchini et al., 2023; Gaucher et al., 2012; Li et al., 2013; Maezawa et al., 2020; Manterola et al., 2018; Ozata et al., 2020; Yu et al., 2021). Additionally, extensive chromatin remodeling takes place in spermatocytes during meiotic prophase I, involving histone variant exchange, histone modifications, and high-order genome rearrangement (Kota and Feil,

2010; Wang et al., 2017; Zheng and Xie, 2019). It has been known that SETDB1-mediated H3K9 trimethylation (H3K9me3) is required for sex chromosome transcription silencing (a process called meiotic sex chromosome inactivation, MSCI) and male meiotic procession (Hirota et al., 2018). However, the specific involvement of chromatin regulators in gene activation on autosomes remains poorly understood.

Zinc finger HIT-type containing 1 (ZNHIT1), an evolutionarily conserved subunit of the SRCAP chromatin remodeling complex, acts as a key regulator for the histone variant H2A.Z deposition to control gene expression and cell fate determination (Cai et al., 2005; Cuadrado et al., 2007; Feng et al., 2022). Recent studies have shown that ZNHIT1 is involved in a wide range of developmental processes, including muscle and lens differentiation, heart development, lung branching, and adult tissue stem cell maintenance (Cuadrado et al., 2010; Lu et al., 2022; Sun et al., 2020; Wei et al., 2022; Xu et al., 2021; Zhao et al., 2019). In our previous study, *Znhit1* deletion in early male germ cells impaired the mitosis-to-meiosis transition by regulating *Meiosin* expression (Sun et al., 2022). However, the in vivo function of ZNHIT1 in regulating meiotic progression remains unknown.

To delve into the function of ZNHIT1 in meiosis, we analyzed *Znhit1* expression and observed upregulation specifically during meiotic prophase. Here, we examine the role of ZNHIT1 in multiple meiotic events and show that *Znhit1* deletion in spermatocytes causes defects of pachytene gene expression, thereby resulting in meiotic developmental arrest. Hence, our study highlights the essential role of ZNHIT1 in ensuring meiotic progression.

Results

Znhit1 expression is upregulated during meiotic prophase and *Znhit1* knockout in spermatocytes disrupts spermatogenesis

To identify potential chromatin regulators in meiosis, we first queried for chromatin factors highly expressed during the zygotene stage based on published scRNA-seq data (Fig S1A and Table S1) (Chen et al., 2018). Quantitative analysis showed that the chromatin remodeler *Znhit1* was among the most highly expressed factors (Fig 1A, B, S1B, C). RNA in situ hybridization validated that *Znhit1* expression in male germ cells decreased after meiotic initiation, followed by a gradual increase in spermatocytes from the zygotene stage to the metaphase stage (Fig 1C). These results suggest that ZNHIT1 is a potential chromatin regulator of meiotic progression.

To investigate whether ZNHIT1 regulates meiotic progression, we generated spermatocyte-specific *Znhit1* knockout mice (*Znhit1*$^{fl/fl}$; *Stra8-cre*, referred to as *Znhit1*-sKO). In the first wave of spermatogenesis, Ngn3-negative prospermatogonia directly differentiate into A2 spermatogonia(Law et al., 2019; Rabbani et al., 2022; Yoshida et al., 2006; Yoshida et al., 2004). With Stra8-cre inducing recombination in A1 spermatogonia and preleptotene spermatocytes separately(Lin et al., 2017), it is feasible to generate mice with spermatocyte-specific gene knockout (Fig 1D). RNA in situ experiments on testis sections confirmed the deletion of *Znhit1* mRNA in spermatocytes (Fig 1E, S1D). Compared with littermate controls, *Znhit1*-sKO male mice had smaller testes (Fig S1E, F). PAS-histological and PNA-fluorescent staining illuminated the absence of round spermatids and elongated spermatids in *Znhit1*-sKO testes (Fig 1F, G), indicating that *Znhit1* knockout in spermatocytes disrupted spermatogenesis.

Znhit1 deletion leads to meiotic arrest at the pachytene stage

To study spermatocyte development in *Znhit1*-sKO testes, we co-stained SYCP3, a marker of primary spermatocytes, and HSPA2, a testis-specific HSP70 family member that accumulates from the pachytene stage onward. Both control and *Znhit1*-sKO testis sections exhibited SYCP3^{+}HSPA2^{+} primary spermatocytes (Fig S2A). Phospho-histone H3 (Thr3) (pH3) is a marker of mitotic and meiotic metaphase cells, and *Znhit1* deletion resulted in the complete absence of pH3^{+} metaphase spermatocytes within the seminiferous tubule lumen (Fig S2B). These results suggest that *Znhit1* deletion arrests spermatocytes in meiotic prophase I.

To pinpoint the onset of meiotic failure, we performed immunostaining against SYCP3 in spermatocyte chromosome spreads. The wild-type testes displayed typical spermatocytes at consecutive substages, including leptotene, zygotene, pachytene, diplotene, and diakinesis (Fig 2A). However, spermatocytes at the diplotene and diakinesis stages were rarely observed in *Znhit1*-sKO testes (Fig 2B, C). We also examined the expression of H1T, a middle pachytene marker, and no difference in H1T expression was observed in *Znhit1*$^{-/-}$ spermatocytes (Fig S2C). *Znhit1* knockout resulted in increased TUNEL-positive spermatocytes, suggesting that these defective spermatocytes were eliminated by the apoptotic pathway (Fig 2D, E). We further performed scRNA-seq analysis of postnatal day 35 (P35) testes from control and *Znhit1*-sKO. Uniform manifold approximation and projection (UMAP) showed that germ cells normally progressed through all meiotic stages and successfully gave rise to spermatids in control groups (Fig 2F). By contrast, in the *Znhit1* knockout group, late pachytene spermatocytes decreased significantly, and only very few subsequent germ cell types were observable. *Pou5f2* is expressed explicitly at the diplotene stage, and we found a lack of *Pou5f2*$^{+}$ diplotene spermatocytes in *Znhit1*-sKO testes (Fig 2G). These results indicate that *Znhit1* deletion leads to meiotic arrest at the pachytene stage.

ZNHIT1 is required for DSB repair and meiotic recombination

To investigate the impact of ZNHIT1 on meiotic events, we first performed immunostaining of SYCP1 and SYCP3, the essential components of the synaptonemal complex, to examine whether ZNHIT1 regulates homologous synapses. Pachytene nuclei with fully synapsed autosomes were observed in spermatocytes from the control (Fig. 3A). In *Znhit1*-sKO testes, while autosomal synapsis appeared grossly normal, abnormalities were present at the terminal ends of autosomes. During the pachytene stage, the X and Y chromosomes undergo pairing and synapses between the short pseudoautosomal regions (PARs). We found an increase in the percentage of unsynapsed X-Y chromosomes in *Znhit1*-sKO spermatocytes (Fig 3B). Thus, deletion of *Znhit1* results in impaired chromosomal synapsis.

Next, we examined the programmed formation and repair of DSBs by co-staining SYCP3 and γH2AX, a DSB marker, on spermatocyte chromosome spreads. In both control and *Znhit1*-sKO spermatocytes, γH2AX signals were evident in the leptotene and zygotene stages (Fig 3C). However, in *Znhit1*-deficient pachynema, we still observed diffuse γH2AX signals on the autosomes, while in control pachynema, γH2AX signals only

accumulated on the X-Y chromosomes. These results demonstrate that ZNHIT1 is required for completing DSB repair.

To understand how ZNHIT1 regulates DSB repair, we performed an immunostaining analysis using the markers RPA2 and RAD51, the essential factors involved in DSB repair. We found an increase in RPA2 and RAD51 counts in both zygonema and pachynema of *Znhit1*-deficient testes (Fig 3D, E, and S3A, B), indicating that *Znhit1* deletion delayed recombinational repair, resulting in defective resolution of autosomal DSBs in *Znhit1*$^{-/-}$ pachynema. The formation and repair of DSBs play crucial roles in initiating and facilitating meiotic recombination, respectively. To examine the consequences of unrepaired DSBs on meiotic recombination in *Znhit1* mutants, we performed an immunostaining analysis against MLH1, a marker of meiotic crossover formation. Indeed, we found an almost absence of MLH1 foci in *Znhit1*$^{-/-}$ pachytene spermatocytes compared with controls (Fig 3F and S3C), indicating that *Znhit1* deletion severely disrupted meiotic crossover formation.

scRNA-seq analysis reveals that *Znhit1* deletion impairs meiotic transcriptional programs

We next investigated whether *Znhit1* deletion impacts meiotic gene expression programs. To address this, we isolated testicular cells from control and *Znhit1*-sKO mice at P16 and performed scRNA-seq analysis. scRNA-seq analysis identified 6 distinct germ cell types based on the expression of canonical stage-specific markers (Chen et al., 2018), including undifferentiated spermatogonia (*Zbtb16*), differentiating spermatogonia (*Kit*), preleptotene spermatocytes (*Nacad*), leptotene spermatocytes (*Meiob*), zygotene spermatocytes (*Psma8*), and pachytene spermatocytes (*Piwil1*) (Fig 4A and S4A, B). We then analyzed the average expression of gene sets dynamically changed during meiotic transitions, including genes upregulated or downregulated at the leptotene-to-preleptotene (Lep/PreL), zygotene-to-leptotene (Zyg/Lep), and pachytene-to-zygotene (Pac/Zyg) stages (Table S2). While *Znhit1* deletion had minimal effects on genes activated or repressed during early meiotic transitions (PreL→Lep and Lep→Zyg), it specifically and severely impaired the transcriptional programs at the zygotene-to-pachytene transition. Specifically, the average expression of 1,560 genes was activated at the pachytene stage (referred to as pachytene-activated genes, or PGA genes), while *Znhit1* deletion downregulated these PGA genes (Fig 4B). Functional enrichment analysis revealed that these PGA genes were primarily involved in DNA repair, cilium organization, and

spermatid development, consistent with the biological process of germ cell development (Table S3).

Moreover, we identified differentially expressed genes (DEGs) in each spermatocyte type between the control and *Znhit1*-sKO groups. The number of DEGs gradually increased from the preleptotene to the pachytene stage, with downregulated genes predominating (Fig 4C and Table S4). In particular, *Znhit1*$^{-/-}$ pachytene spermatocytes exhibited 2,785 downregulated genes, among which were most of the pachytene-activated genes (1,094 out of 1,560, 70.1%). Functional enrichment analysis revealed that upregulated genes following *Znhit1* deletion were associated with apoptotic pathways, supporting an observation that *Znhit1* deletion resulted in germ cell clearance through apoptosis (Fig 4D). Moreover, downregulated GO terms included germ cell development and DNA recombination (Fig 4E and Table S5). Interestingly, recent studies showed that cilium organization was essential for spermatocyte development (Mytlis et al., 2022), and *Znhit1* deletion reduced the expression of cilium-related genes in zygotene and pachytene spermatocytes (Fig 4E). We further conducted bulk RNA-seq experiments with P14 control and *Znhit1*-sKO testicular cells and identified 882 DEGs (812 downregulated genes and 70 upregulated genes) in *Znhit1*-sKO testicular cells (Fig S5A, and Table S6). Through integrative analysis of bulk and single-cell RNA-seq data, we found that the expression of these 812 genes was activated during the zygotene-to-pachytene transition, and *Znhit1* deletion significantly reduced the expression of these genes (Fig S5B). We also analyzed the expression of XY-linked genes. As shown in Figure 4F, while only modest numbers of XY-DEGs were detected at preleptotene and leptotene, a striking accumulation of upregulated XY-DEGs was observed at zygotene (120 genes) and pachytene (119 genes). This aberrant activation of XY-linked genes directly reveals a failure of Meiotic Sex Chromosome Inactivation (MSCI) in *Znhit1*-knockout spermatocytes. Together, these data indicate that ZNHIT1 is essential for the regulation of meiotic transcriptional programs.

Consistent with meiotic recombination defects in *Znhit1* mutants, genes associated with homologous recombination were repressed following *Znhit1* deletion, including *Ccnb1ip1*, *Rnf212*, *Spo16*, *Ankrd31*, and *Terb1* (Boekhout et al., 2019; Papanikos et al., 2019; Qiao et al., 2014; Rao et al., 2017; Reynolds et al., 2013; Shibuya et al., 2014; Wang et al., 2019; Zhang et al., 2019) (Fig S5C, D).

Znhit1 deletion impairs H2A.Z incorporation into pachytene chromatin

We then asked how ZNHIT1 regulates transcription. ZNHIT1 is a subunit of the SRCAP complex that facilitates the incorporation of the histone variant H2A.Z by replacing H2A (Fig S6A)(Yu et al., 2024). Immunostaining against H2A.Z showed a gradual increase in H2A.Z accumulation on autosomes from the leptotene to the diakinesis stage, while the H2A.Z signal was markedly low on the X-Y body (Fig 5A). *Znhit1* loss decreased H2A.Z staining on the pachytene cells, suggesting that ZNHIT1 is required for maintaining H2A.Z integrity during meiosis.

To profile H2A.Z target genes, we performed chromatin immunoprecipitation followed by sequencing (ChIP-seq) against H2A.Z in P14 testicular cells. Using the ChromHMM model to annotate H2A.Z signals with meiocyte chromatin states defined by published epigenetic markers (Spruce et al., 2020), we found that H2A.Z sites were primarily enriched in chromatin state 1 and state 2 (promoters and enhancers) but were less enriched in recombination hotspots (Fig 5B, C), consistent with previously published results (Spruce et al., 2020). Quantitative analysis showed significant H2A.Z reduction at 37.9% (23,926 of 63,109) of H2A.Z-bound genome sites following *Znhit1* deletion (Fig 5D). Comparison analysis with bulk RNA-seq data identified 480 downregulated DEGs with decreased H2A.Z signals (Fig 5E). ~41.3 and 37.8% of the downregulated H2A.Z peaks occupied promoters and enhancers, respectively. At promoters, these downregulated H2A.Z preferentially occupied active promoters (H3K4me3 only), while H2A.Z occupied three types of enhancers: active, poised, and primed enhancers (Fig 5F, and S6B, C). These findings indicate that *Znhit1* deletion impairs H2A.Z incorporation into pachytene chromatin.

H2A.Z deposition cooperates with A-MYB to regulate transcription

We further asked how ZNHIT1/H2A.Z deposition facilitates lineage-specific gene expression. We performed TF motif analysis using active promoters/enhancers with decreased H2A.Z signals. This analysis identified several MYB family TFs, including MYB, A-MYB, and B-MYB (Fig 6A). Gene regulatory network analysis conducted by SCENIC further identified A-MYB (encoded by the *Mybl1* gene) as the core regulatory TF in spermatocytes (Fig 6B). We reanalyzed RNA-seq data in P14 testes from A-MYB-deficient mice (Li et al., 2013) and found that A-MYB-deficient DEGs correlated with those observed in *Znhit1*-deficient testicular cells (Fig 6C). Although *Znhit1* deletion didn't affect *Mybl1* mRNA expression, transcriptome analyses showed that the expression of A-MYB target genes was significantly reduced in *Znhit1*$^{-/-}$

pachytene spermatocytes (Fig 6D, E, and S7A). These results suggest that *Znhit1*$^{-/-}$ and *Mybl1*$^{-/-}$ pachytene spermatocytes share common gene expression alterations.

Next, we compared the genome binding sites of H2A.Z and A-MYB. Utilizing published A-MYB ChIP-seq data from P14 testicular cells (Li et al., 2013), we identified 6,088 A-MYB binding signals, with 78.1% (4755) of these coinciding with H2A.Z peaks (Fig 6F). Annotation of genomic features showed that approximately 66.52% and 12.02% of these overlapping sites occupied active promoters and enhancers, respectively, representing a stronger enrichment compared to other regulatory elements (Fig 6G). Genes associated with H2A.Z and A-MYB binding included essential HR-related genes, such as *Ccnb1ip1* (Fig 6H). Moreover, we showed that *Znhit1* deletion resulted in a marked reduction in H2A.Z signals and nascent transcription identified by KAS-seq signals (Fig 6I). We further linked KAS□seq signals with gene expression profiles, and found that *Znhit1* depletion caused a global reduction in KAS□seq signals, especially at promoters of downregulated genes (Fig S8A), indicating defective transcription bubble formation. In comparison, genes with increased expression showed low KAS□seq signals in both control and mutant groups, likely reflecting indirect regulation. These results further support the essential role of ZNHIT1 in transcriptional regulation.

Previous studies have shown the fundamental role of A-MYB in activating meiotic enhancers (Maezawa et al., 2020). We found that *Znhit1* deletion resulted in reduced KAS-seq signals at active enhancers (Fig 6I). Interestingly, the chromatin accessibility detected by ATAC-seq at active enhancers increased after *Znhit1* deletion, suggesting that *Znhit1* deletion results in dysregulated chromatin state. These findings suggest that ZNHIT1/H2A.Z deposition is essential for enhancer activation.

Together, these results demonstrate the critical role of the ZNHIT1/H2A.Z/A-MYB axis in governing meiotic transcriptional programs.

Discussion

Meiosis plays a crucial role in the production of haploid gametes. Any disturbances during meiotic progress are known to lead to infertility and congenital diseases. Here we delineate the multifaceted functions of the chromatin remodeler ZNHIT1 in regulating meiotic progression. Our study provides convincing data to show that the ZNHIT1/H2A.Z/A-MYB axis controls spermatocyte development, meiotic recombination, and PGA. Thus, these findings underscore the significance of specific chromatin structures in governing appropriate transcriptional reprogramming and precise meiotic progression.

The role of H2A.Z in DNA injury and repair has been extensively studied (Colino-Sanguino et al., 2022; Dong et al., 2014; Xu et al., 2012; Yamada et al., 2018), but its function in programmed DSB formation and repair during mammalian meiosis remains unknown. To address this question, we generated *Znhit1* conditional knockout mice specifically during male meiosis to examine the role of ZNHIT1-mediated H2A.Z deposition in the formation and repair of programmed DSB. One new observation in this study is that *Znhit1* loss is dispensable for DSB formation but necessary for DNA break repair during meiosis. Intriguingly, unlike the observations in plant meiosis but consistent with Christopher L. Baker's group observation in mouse, we confirmed that H2A.Z does not directly bind DNA recombination sites in mammalian spermatocytes (Choi et al., 2013; Spruce et al., 2020; Wang and Copenhaver, 2018). Moreover, we showed that *Znhit1* deletion delays recombinational repair but has limited impacts on DNA resection, ultimately causing defective meiotic crossover formation. Importantly, our study demonstrates that ZNHIT1 is essential for the expression of meiotic recombination-related genes, such as *Ccnb1ip1* and *Rnf212*, implying that ZNHIT1/H2A.Z modulates meiotic recombination through transcriptional regulation, rather than a direct regulatory effect of ZNHIT1 on recombination machinery. Therefore, our data reveal a different mechanism underlying meiotic recombination between plants and mammals.

Pachytene spermatocytes utilize a highly specific mechanism of meiotic surveillance, the pachytene checkpoint, to prevent aneuploidy formation by removing abnormal germ cells with incomplete chromosome synapsis and defective homologous recombination (Huang and Roig, 2023; Roeder and Bailis, 2000; Subramanian and Hochwagen, 2014). Two checkpoint pathways exist in male meiosis: one responding to unrepaired DSBs and the

other triggered by MSCI failure (Royo et al., 2013). However, whether epigenetic regulation is involved in meiotic surveillance is not well defined. Previous studies have reported that upon stimulation by unrepaired DSBs, the MRE11-ATM-CHK2 pathway is activated to eliminate aberrant germ cells (Marcet-Ortega et al., 2017). Our study found that *Znhit1* deletion impairs pachytene development and XY-linked gene repression, ultimately causing meiotic pachytene arrest and apoptosis. Therefore, these findings demonstrate that ZNHIT1 acts as an important chromatin factor involved in the regulation of the pachytene checkpoint.

It has long been noticed that in meiotic prophase I, chromatin that has not yet completed chromosomal synapses is transcriptionally inactive, known as meiotic silencing of unsynapsed chromatin (MSUC) (Turner et al., 2005). When germ cells enter the pachytene stage, a large number of protein-coding genes and non-coding RNAs begin to be actively expressed, known as PGA. Previous studies have shown that transcription factors A-MYB and BRDT are involved in transcriptional activation during meiotic prophase, but how PGA takes place in the chromatin context is unclear. In this study, we found that the expression of the chromatin remodeler Znhit1 is specifically upregulated during the zygotene-to-pachytene transition. We also observed that H2A.Z deposition is enriched in the autosomes but less in the sex chromosomes at the pachytene stage. *Znhit1* deletion in spermatocytes repressed pachytene gene activation globally and reduced chromosome-wide H2A.Z deposition, supporting a central role of ZNHIT1 in PGA regulation and chromatin remodeling. It has been known that A-MYB is a transcription factor that controls pachytene transcription activation. We found that *Znhit1*-deficient spermatocytes phenocopied abnormal meiotic phenotypes observed in A-MYB mutants, such as X-Y synapsis failure, impaired DSB repair, and defective HR (Alexander et al., 2023; Bolcun-Filas et al., 2011; Li et al., 2013; Maezawa et al., 2020). Our results also revealed that ZNHIT1/H2A.Z cooperates with A-MYB to regulate PGA gene activation. Therefore, our study illuminates the molecular mechanisms underlying the fundamental question of how PGA is regulated.

The histone variant H2A.Z is enriched at gene promoters and regulatory regions, yet there is ongoing debate about its role in transcriptional regulation. A recent paper reported that H2A.Z knockout in post-mitotic muscle cells has limited effects on gene expression (Belotti et al., 2020). In this study, we utilized the meiotic prophase as a model system (where DNA replication does not occur) to study H2A.Z's function in transcriptional

regulation. We found that ZNHIT1-mediated H2A.Z deposition, independent of DNA replication, is indispensable for the transcriptional activation of a large number of meiotic genes. One explanation of this conflicting phenomenon is that H2A.Z dynamics, but not stable H2A.Z accumulation is essential for priming transcriptional changes.

Through the integration of functional and molecular evidence, our findings establish the critical involvement of ZNHIT1-dependent chromatin remodeling in the orchestration of meiotic progression and coordination of various meiotic processes, such as HR and PGA. Furthermore, we pinpoint the pivotal role played by the ZNHIT1/H2A.Z/A-MYB axis in driving transcriptional reprogramming during meiotic prophase. Taken together, this study deepens our understanding of the interplay between epigenetic regulation and mammalian meiosis.

Materials and Methods

Animals. *Znhit1*$^{fl/fl}$ mice have been previously described (Zhao et al., 2019) and are available from the Model Animal Research Center of Nanjing University (MARC, Nanjing, China). The *Stra8-cre* knock-in mouse line was kindly provided by Dr. Ming-Han Tong(Lin et al., 2017). All mice were maintained on the C57BL/6J background. Germ cell-specific *Znhit1* knockout mice (*Znhit1*$^{fl/fl}$; *Stra8-cre*) were obtained by crossing *Znhit1*$^{fl/+}$; *Stra8-cre* mice with *Znhit1*$^{fl/fl}$ mice. All mice were housed in the SPF (Specific-Pathogen-Free) animal facility with standard 12 h light/dark cycles and standard temperature (22 to 24□). All mice were provided with ad libitum access to standard laboratory food and water. All experiments in this study were performed following relevant guidelines and approved by the Animal Care and Use Committee of Fudan University.

Histological and immunohistochemical analysis. Testes were fixed in modified Davidson's fixative as previously described (Latendresse et al., 2002), embedded in paraffin, and sectioned. For periodic acid-Schiff (PAS)-hematoxylin staining, 5 μm testis sections were deparaffinized, rehydrated, and stained with Schiff's reagent and hematoxylin solution. For immunofluorescent staining, 5 μm testis sections were retrieved by sodium citrate antigen retrieval buffer (pH 6.0) and blocked with 5% BSA in PBS for 30 min at room temperature. The sections were later incubated overnight at 4°C with primary antibodies as follows: mouse anti-SYCP3 (Abcam, ab97672), rabbit anti-HSPA2 (Abcam, ab108416), rabbit anti-pH3 (Millipore, H0412), rabbit anti-H1T (Invitrogen, PA5-51200), or lectin PNA (Sigma□Aldrich, L7381). On the following day, secondary fluorescein-conjugated antibodies and DAPI (Sigma□Aldrich, D9542) were added for 1 h, followed by Fluoromount-G mounting (Southern Biotech, 0100-01). Images were analyzed using the confocal microscope.

TUNEL staining was carried out using the DeadEnd^{TM} Fluorometric TUNEL System (Promega, G3250) according to the manufacturer's instructions.

Immunostaining of spermatocyte chromosome spreads. Spermatocyte chromosome spreads were prepared as previously described (Alavattam et al., 2018). Briefly, the clumps of seminiferous tubules were transferred to the hypotonic extraction buffer (30 mM Tris base, 17 mM trisodium citrate, 5 mM EDTA, 50 mM sucrose, 5 mM dithiothreitol (DTT), and 1× protease inhibitor, pH 8.2) and incubated on ice for 1.5 h. The clumps of tubules were then transferred to 30 μL of ice-cold 100 mM sucrose and mashed gently using tweezers to obtain a cell suspension. An additional 30 μL of ice-cold 100 mM sucrose was added to the cell suspension and mixed several times. Positively charged slides were incubated in the ice-cold fixation solution (2% paraformaldehyde, 0.1% Triton X-100, and 0.02% SDS, pH 9.2) for 3 min. 30 μL of the diluted cell suspension was applied to the slides and incubated in humid chambers at room temperature for 2 h. The slides were washed with 0.4% Photo-Flo 200 and stored at -80□.

For immunostaining of spermatocyte chromosome spreads, slides were washed with PBS and blocked with 5% BSA in PBS for 30 min at room temperature. The slides were stained with primary antibodies as follows: rabbit anti-SYCP3 (Abcam, ab15093), mouse anti-SYCP3 (Abcam, ab97672), rabbit anti-SYCP1 (Abcam, ab15090), mouse anti-γH2AX (BioLegend, 613401), rabbit anti-RAD51 (Proteintech, 14961-1-AP), rabbit anti-RPA2 (Proteintech, 10412-1-AP), rabbit anti-MLH1 (Cell Signaling Technology, 3515T), rabbit anti-H2A.Z (Abcam, ab4174).

***Znhit1* in situ hybridization.** Testis sections (5 μM) at the indicated times were prepared for *Znhit1* in situ hybridization with the RNAscope kit (Advanced Cell Diagnostics, 323100) according to the manufacturer's instructions.

Quantitative reverse transcription PCR (RT-qPCR). Total RNA was isolated using the RNeasy Mini-plus Kit (Qiagen, 74134) and then reverse-transcribed into complementary DNA (cDNA) with the GoScript Reverse Transcription System (Promega, A5003). cDNA was used as the template for the quantitative PCR assay using 2×SYBR Green qPCR Master Mix (Bimake, B21202). Quantitative PCR primers are listed in Table S7.

RNA-seq library generation and sequencing. Total RNA from fresh testes was isolated and mRNA was purified with magnetic beads (Vazyme, N401-01). Then, mRNA was fragmented and processed to generate RNA-seq libraries (Vazyme, NR605-01). Over 40 million reads were obtained per sample using the Illumina NovaSeq platform for 2 independent biological replicates.

Single-cell RNA sequencing (scRNA-seq). P16 and P35 control and *Znhit1*-sKO testes were digested by collagenase IV and trypsin at 37□ for 10 min to obtain testicular cell suspensions. scRNA-seq libraries were constructed using a 10x Genomics kit and sequenced on the Illumina platform.

ChIP-seq library generation and sequencing. ChIP-seq library generation was performed as previously described. Briefly, P14 control and *Znhit1*-sKO testes were digested by collagenase IV and trypsin at 37□ for 10 min, crosslinked with 1% formaldehyde for 10 min, and quenched with glycine. The cells were lysed and sheared with a Bioruptor Plus machine for 20 min. Then, 2 μg of anti-H2A.Z antibody (Abcam, ab4174) was added to the sonicated chromatin and incubated overnight at 4□. The following day, 20 μL of protein G beads were added and incubated for 2 h at 4□. The beads were washed and reverse-crosslinked for 4 h at 65□. DNA was extracted using phenol-chloroform and subjected to library construction using the VAHTS Universal DNA Library Prep Kit for Illumina (Vazyme, ND607-01) according to the manufacturer's instructions. Over 30 million reads were obtained per sample using the Illumina NovaSeq platform for 2 independent biological replicates.

KAS-seq library and ATAC-seq library generation and sequencing. Testes were digested by collagenase IV and trypsin at 37□ for 10 min. Pachytene cells were sorted using fluorescence-activated cell sorting (FACS) as previously described (Long et al., 2017). For KAS-seq, pachytene cells were labeled with N3-kethoxal, and DNA was isolated using the DNA Clean and Concentrator kit (Zymo, D4013) and subjected to library construction using Q5 high-fidelity DNA polymerase (New England Biolabs, M0544S). Genomic DNA was fragmented using Tn5 transposase and subjected to library

construction. For ATAC-seq, pachytene nuclei were isolated and fragmented with Tn5 transposase. DNA was isolated using the DNA Clean and Concentrator kit (Zymo, D4013) and subjected to library construction using Q5 high-fidelity DNA polymerase (New England Biolabs, M0544S). For high-throughput sequencing, over 30 million reads were obtained per sample using the Illumina NovaSeq platform for 2 independent biological replicates.

RNA-seq data analysis. We performed RNA-seq analysis as described previously (Pertea et al., 2016). Briefly, after removing adapters using Cutadapt (v2.5) (Kechin et al., 2017), paired-end reads were aligned to the annotated mouse transcripts (mm10 Gencode vM23 release) using Hisat2 (v2.2.1) (Kim et al., 2015; Kim et al., 2019). Gene expression levels were calculated using StringTie (v2.2.1) (Pertea et al., 2015). Read counts were calculated using a Python script (prepDE.py3) provided by the StringTie development team. Differentially expressed genes were identified using the R package DESeq2 (v1.38.3) (Love et al., 2014). Genes with read counts > 50 in at least one sample were kept for further analysis. A given gene was considered to significantly changed if the adjusted P value (padj) was < 0.05, the P value was < 0.01, and the fold-change was≥ 2. Gene Set Enrichment Analysis (GSEA) was carried out using GSEA software (Subramanian et al., 2005). GO analysis was performed using clusterProfiler (v4.6.2) (Wu et al., 2021).

scRNA-seq data analysis. FASTQ files were run through CellRanger (v7.1.0) software with default parameters for de-multiplexing, aligning reads with STAR software to mm10, and counting unique molecular identifiers (UMIs). As input files of the Seurat R package (v4.4.0), the filtered gene expression matrices were then used for downstream analyses (Butler et al., 2018). Low-quality cells were filtered (expressing < 500 or >6,000 unique gene counts and >15% mitochondrial reads). Principal component analysis was performed on SCT-transformed data using 3,000 variable genes. The top 50 principal components were used for clustering and visualized using the UMAP algorithm in the Seurat R package. The "FindAllMarkers" function of the Seurat R package was used to calculate

cluster-specific genes. Marker genes for each cluster are shown in Table S8.

The "FindMarkers" function of the Seurat R package was used to identify differentially expressed genes (DEGs) for spermatocytes (preleptotene, leptotene, zygotene, and pachytene). Only those with |'avg_logFC'| > 0.25 and 'p_val_adj' < 0.05 were considered as DEGs. For the transcriptional regulatory network analysis, the raw count matrix was used by the pyscenic (v0.12.1) workflow using default parameters (Aibar et al., 2017). Then, the output loom file was opened by the SCENIC R package (v1.3.1), and AUC values of regulons were extracted for visualization of downstream transcription factor activity.

ChIP-seq and KAS-seq data analysis. For analyzing ChIP-seq and KAS-seq data, we used the ENCODE ChIP-seq pipeline (v2.2.1, https://github.com/ENCODE-DCC/chip-seq-pipeline2). Raw reads were cleaned by Cutadapt (v2.5) (Kechin et al., 2017). After removing adapters, clean reads were aligned against the mouse mm10 genome using bwa (v0.7.17) (Li and Durbin, 2009). Then, sam files were converted to bam files using samtools (v1.9) (Li et al., 2009). PCR duplicates were removed using Picard (v2.20.7) (https://broadinstitute.github.io/picard/). Histone ChIP-seq peaks (such as H2A.Z and histone marks) and KAS-seq peaks were called using MACS2 (v2.2.4) (Zhang et al., 2008), while transcription factor ChIP-seq peaks (such as A-MYB) were called using the R packages spp (v1.15.5) (https://github.com/hms-dbmi/spp). The conservative narrow peaks were used for downstream analysis.

For visualization, bam files were converted to bigWig files using deepTools (v3.3.1) (Ramirez et al., 2014), and bigWig files were used to calculate tag density under 50 bp resolution. In addition, CPM was used to normalize the number of reads per bin. We used the R package DiffBind (v3.8.4) (http://bioconductor.org/packages/release/bioc/html/DiffBind.html) for differential peak analysis and the R package rGREAT (v2.1.11) (Gu and Hubschmann, 2023) for peak annotation. We used ComputeMatrix and plotHeatmap of deepTools to generate count

matrices and heatmaps, respectively. H2A.Z enrichment within chromatin states was annotated using the ChromHMM model (Ernst and Kellis, 2012; Spruce et al., 2020). TF motif enrichment was calculated using HOMER (v4.11) (Heinz et al., 2010). We used deepTools to draw Pearson's correlation scatter plots for the correlation between replicates of each experiment.

For promoter and enhancer type analysis, H3K27ac ChIP-seq data in wild-type pachytene spermatocytes were downloaded from the published data (GSE107398) (Adams et al., 2018); ChIP-seq data for H3K4me1, H3K4me3, and H3K27me3 in wild-type pachytene spermatocytes were downloaded from the published data (GSE132446) (Chen et al., 2020).

ATAC-seq data analysis. ATAC-seq data were analyzed using a standardized ENCODE ATAC-seq pipeline (v2.2.2, https://github.com/ENCODE-DCC/atac-seq-pipeline). The mouse reference genome (mm10) was used in the pipeline. Trimming, mapping, and duplicate-removing were performed as the ENCODE pipeline suggested using Cutadapt (v2.5) (Kechin et al., 2017), Bowtie2 (v2.3.4.3) (Langmead et al., 2009), and Picard (v2.20.7) (https://broadinstitute.github.io/picard/) respectively. MACS2 (v2.2.4) (Zhang et al., 2008) was used for peak calling.

Statistics and reproducibility. Statistical analyses were performed using R and Prism 9. Data are presented as means ± s.d. unless otherwise indicated. The two-tailed, unpaired, Student's t-test, Mann–Whitney test, or one-way or two-way ANOVA were performed to analyze statistical significance.

Supplementary Materials

This manuscript file includes Figs. S1 to S9 and Tables S1 and S8.

Reference

Adams, S.R., Maezawa, S., Alavattam, K.G., Abe, H., Sakashita, A., Shroder, M., Broering, T.J., Sroga Rios, J., Thomas, M.A., Lin, X.*, et al.* (2018). RNF8 and SCML2 cooperate to regulate ubiquitination and H3K27 acetylation for escape gene activation on the sex chromosomes. PLoS genetics *14*, e1007233.

Aibar, S., Gonzalez-Blas, C.B., Moerman, T., Huynh-Thu, V.A., Imrichova, H., Hulselmans, G., Rambow, F., Marine, J.C., Geurts, P., Aerts, J.*, et al.* (2017). SCENIC: single-cell regulatory network inference and clustering. Nature methods *14*, 1083-1086.

Alavattam, K.G., Abe, H., Sakashita, A., and Namekawa, S.H. (2018). Chromosome Spread Analyses of Meiotic Sex Chromosome Inactivation. Methods in molecular biology (Clifton, NJ) *1861*, 113-129.

Alexander, A.K., Rice, E.J., Lujic, J., Simon, L.E., Tanis, S., Barshad, G., Zhu, L., Lama, J., Cohen, P.E., and Danko, C.G. (2023). A-MYB and BRDT-dependent RNA Polymerase II pause release orchestrates transcriptional regulation in mammalian meiosis. Nature communications *14*.

Baudat, F., Imai, Y., and de Massy, B. (2013). Meiotic recombination in mammals: localization and regulation. Nature reviews Genetics *14*, 794-806.

Belotti, E., Lacoste, N., Simonet, T., Papin, C., Padmanabhan, K., Scionti, I., Gangloff, Y.G., Ramos, L., Dalkara, D., Hamiche, A.*, et al.* (2020). H2A.Z is dispensable for both basal and activated transcription in post-mitotic mouse muscles. Nucleic acids research *48*, 4601-4613.

Bergerat, A., de Massy, B., Gadelle, D., Varoutas, P.C., Nicolas, A., and Forterre, P. (1997). An atypical topoisomerase II from Archaea with implications for meiotic recombination. Nature *386*, 414-417.

555 Boekhout, M., Karasu, M.E., Wang, J., Acquaviva, L., Pratto, F., Brick, K., Eng, D.Y., Xu, J.,
556 Camerini-Otero, R.D., Patel, D.J., *et al.* (2019). REC114 Partner ANKRD31 Controls Number,
557 Timing, and Location of Meiotic DNA Breaks. Molecular cell *74*, 1053-1068 e1058.
558 Bolcun-Filas, E., Bannister, L.A., Barash, A., Schimenti, K.J., Hartford, S.A., Eppig, J.J.,
559 Handel, M.A., Shen, L., and Schimenti, J.C. (2011). A-MYB (MYBL1) transcription factor is a
560 master regulator of male meiosis. Development *138*, 3319-3330.
561 Butler, A., Hoffman, P., Smibert, P., Papalexi, E., and Satija, R. (2018). Integrating single-cell
562 transcriptomic data across different conditions, technologies, and species. Nature
563 biotechnology *36*, 411-420.
564 Cai, Y., Jin, J., Florens, L., Swanson, S.K., Kusch, T., Li, B., Workman, J.L., Washburn, M.P.,
565 Conaway, R.C., and Conaway, J.W. (2005). The mammalian YL1 protein is a shared subunit
566 of the TRRAP/TIP60 histone acetyltransferase and SRCAP complexes. The Journal of
567 biological chemistry *280*, 13665-13670.
568 Cecchini, K., Biasini, A., Yu, T., Saflund, M., Mou, H., Arif, A., Eghbali, A., Colpan, C.,
569 Gainetdinov, I., de Rooij, D.G., *et al.* (2023). The transcription factor TCFL5 responds to
570 A-MYB to elaborate the male meiotic program in mice. Reproduction *165*, 183-196.
571 Chen, Y., Lyu, R.T., Rong, B.W., Zheng, Y.X., Lin, Z., Dai, R.F., Zhang, X., Xie, N.N., Wang,
572 S.Q., Tang, F.C., *et al.* (2020). Refined spatial temporal epigenomic profiling reveals intrinsic
573 connection between PRDM9-mediated H3K4me3 and the fate of double-stranded breaks. Cell
574 research *30*, 256-268.
575 Chen, Y., Zheng, Y., Gao, Y., Lin, Z., Yang, S., Wang, T., Wang, Q., Xie, N., Hua, R., Liu, M.,
576 *et al.* (2018). Single-cell RNA-seq uncovers dynamic processes and critical regulators in

577 mouse spermatogenesis. Cell research *28*, 879-896.

578 Choi, K., Zhao, X., Kelly, K.A., Venn, O., Higgins, J.D., Yelina, N.E., Hardcastle, T.J.,

579 Ziolkowski, P.A., Copenhaver, G.P., Franklin, F.C., *et al.* (2013). Arabidopsis meiotic

580 crossover hot spots overlap with H2A.Z nucleosomes at gene promoters. Nature genetics *45*,

581 1327-1336.

582 Colino-Sanguino, Y., Clark, S.J., and Valdes-Mora, F. (2022). The H2A.Z-nuclesome code in

583 mammals: emerging functions. Trends in genetics : TIG *38*, 273-289.

584 Cuadrado, A., Corrado, N., Perdiguero, E., Lafarga, V., Munoz-Canoves, P., and Nebreda,

585 A.R. (2010). Essential role of p18Hamlet/SRCAP-mediated histone H2A.Z chromatin

586 incorporation in muscle differentiation. The EMBO journal *29*, 2014-2025.

587 Cuadrado, A., Lafarga, V., Cheung, P.C., Dolado, I., Llanos, S., Cohen, P., and Nebreda, A.R.

588 (2007). A new p38 MAP kinase-regulated transcriptional coactivator that stimulates

589 p53-dependent apoptosis. The EMBO journal *26*, 2115-2126.

590 Dong, S., Han, J., Chen, H., Liu, T., Huen, M.S., Yang, Y., Guo, C., and Huang, J. (2014). The

591 Human SRCAP Chromatin Remodeling Complex Promotes DNA-End Resection. Current

592 biology : CB *24*, 2097-2110.

593 Ernst, C., Eling, N., Martinez-Jimenez, C.P., Marioni, J.C., and Odom, D.T. (2019). Staged

594 developmental mapping and X chromosome transcriptional dynamics during mouse

595 spermatogenesis. Nature communications *10*, 1251.

596 Ernst, J., and Kellis, M. (2012). ChromHMM: automating chromatin-state discovery and

597 characterization. Nature methods *9*, 215-216.

598 Feng, Y., Zhang, Y., Lin, Z., Ye, X., Lin, X., Lv, L., Lin, Y., Sun, S., Qi, Y., and Lin, X. (2022).

599 Chromatin remodeler Dmp18 regulates apoptosis by controlling H2Av incorporation in
600 Drosophila imaginal disc development. PLoS genetics *18*, e1010395.
601 Gaucher, J., Boussouar, F., Montellier, E., Curtet, S., Buchou, T., Bertrand, S., Hery, P.,
602 Jounier, S., Depaux, A., Vitte, A.L.*, et al.* (2012). Bromodomain-dependent stage-specific male
603 genome programming by Brdt. The EMBO journal *31*, 3809-3820.
604 Gray, S., and Cohen, P.E. (2016). Control of Meiotic Crossovers: From Double-Strand Break
605 Formation to Designation. Annu Rev Genet *50*, 175-210.
606 Green, C.D., Ma, Q., Manske, G.L., Shami, A.N., Zheng, X., Marini, S., Moritz, L., Sultan, C.,
607 Gurczynski, S.J., Moore, B.B.*, et al.* (2018). A Comprehensive Roadmap of Murine
608 Spermatogenesis Defined by Single-Cell RNA-Seq. Developmental cell *46*, 651-667 e610.
609 Gu, Z., and Hubschmann, D. (2023). rGREAT: an R/bioconductor package for functional
610 enrichment on genomic regions. Bioinformatics *39*.
611 Handel, M.A., and Schimenti, J.C. (2010). Genetics of mammalian meiosis: regulation,
612 dynamics and impact on fertility. Nature reviews Genetics *11*, 124-136.
613 Hassold, T., and Hunt, P. (2001). To err (meiotically) is human: the genesis of human
614 aneuploidy. Nature reviews Genetics *2*, 280-291.
615 Heinz, S., Benner, C., Spann, N., Bertolino, E., Lin, Y.C., Laslo, P., Cheng, J.X., Murre, C.,
616 Singh, H., and Glass, C.K. (2010). Simple combinations of lineage-determining transcription
617 factors prime cis-regulatory elements required for macrophage and B cell identities. Molecular
618 cell *38*, 576-589.
619 Hirota, T., Blakeley, P., Sangrithi, M.N., Mahadevaiah, S.K., Encheva, V., Snijders, A.P.,
620 Ellnati, E., Ojarikre, O.A., de Rooij, D.G., Niakan, K.K.*, et al.* (2018). SETDB1 Links the Meiotic

621 DNA Damage Response to Sex Chromosome Silencing in Mice. Developmental cell *47*,
622 645-+.
623 Huang, Y., and Roig, I. (2023). Genetic control of meiosis surveillance mechanisms in
624 mammals. Front Cell Dev Biol *11*, 1127440.
625 Hunter, N. (2015). Meiotic Recombination: The Essence of Heredity. Cold Spring Harbor
626 perspectives in biology *7*.
627 Kechin, A., Boyarskikh, U., Kel, A., and Filipenko, M. (2017). cutPrimers: A New Tool for
628 Accurate Cutting of Primers from Reads of Targeted Next Generation Sequencing. J Comput
629 Biol *24*, 1138-1143.
630 Keeney, S., Giroux, C.N., and Kleckner, N. (1997). Meiosis-specific DNA double-strand breaks
631 are catalyzed by Spo11, a member of a widely conserved protein family. Cell *88*, 375-384.
632 Kim, D., Langmead, B., and Salzberg, S.L. (2015). HISAT: a fast spliced aligner with low
633 memory requirements. Nature methods *12*, 357-360.
634 Kim, D., Paggi, J.M., Park, C., Bennett, C., and Salzberg, S.L. (2019). Graph-based genome
635 alignment and genotyping with HISAT2 and HISAT-genotype. Nature biotechnology *37*,
636 907-915.
637 Kota, S.K., and Feil, R. (2010). Epigenetic transitions in germ cell development and meiosis.
638 Developmental cell *19*, 675-686.
639 Langmead, B., Trapnell, C., Pop, M., and Salzberg, S.L. (2009). Ultrafast and memory-efficient
640 alignment of short DNA sequences to the human genome. Genome biology *10*, R25.
641 Lascarez-Lagunas, L., Martinez-Garcia, M., and Colaiacovo, M. (2020). SnapShot: Meiosis -
642 Prophase I. Cell *181*, 1442-1442 e1441.

643 Latendresse, J.R., Warbrittion, A.R., Jonassen, H., and Creasy, D.M. (2002). Fixation of testes
644 and eyes using a modified Davidson's fluid: comparison with Bouin's fluid and conventional
645 Davidson's fluid. Toxicol Pathol *30*, 524-533.
646 Law, N.C., Oatley, M.J., and Oatley, J.M. (2019). Developmental kinetics and transcriptome
647 dynamics of stem cell specification in the spermatogenic lineage. Nature communications *10*,
648 2787.
649 Li, H., and Durbin, R. (2009). Fast and accurate short read alignment with Burrows-Wheeler
650 transform. Bioinformatics *25*, 1754-1760.
651 Li, H., Handsaker, B., Wysoker, A., Fennell, T., Ruan, J., Homer, N., Marth, G., Abecasis, G.,
652 Durbin, R., and Genome Project Data Processing, S. (2009). The Sequence Alignment/Map
653 format and SAMtools. Bioinformatics *25*, 2078-2079.
654 Li, X.Z., Roy, C.K., Dong, X., Bolcun-Filas, E., Wang, J., Han, B.W., Xu, J., Moore, M.J.,
655 Schimenti, J.C., Weng, Z.*, et al.* (2013). An ancient transcription factor initiates the burst of
656 piRNA production during early meiosis in mouse testes. Molecular cell *50*, 67-81.
657 Lin, Z., Hsu, P.J., Xing, X., Fang, J., Lu, Z., Zou, Q., Zhang, K.J., Zhang, X., Zhou, Y., Zhang,
658 T.*, et al.* (2017). Mettl3-/Mettl14-mediated mRNA N6-methyladenosine modulates murine
659 spermatogenesis. Cell research.
660 Long, J., Huang, C., Chen, Y., Zhang, Y., Shi, S., Wu, L., Liu, Y., Liu, C., Wu, J., and Lei, M.
661 (2017). Telomeric TERB1-TRF1 interaction is crucial for male meiosis. Nat Struct Mol Biol *24*,
662 1073-1080.
663 Love, M.I., Huber, W., and Anders, S. (2014). Moderated estimation of fold change and
664 dispersion for RNA-seq data with DESeq2. Genome biology *15*, 550.

665 Lu, J., An, J., Wang, J., Cao, X., Cao, Y., Huang, C., Jiao, S., Yan, D., Lin, X., and Zhou, X.
666 (2022). Znhit1 Regulates p21Cip1 to Control Mouse Lens Differentiation. Investigative
667 ophthalmology & visual science *63*, 18.
668 Maezawa, S., Sakashita, A., Yukawa, M., Chen, X., Takahashi, K., Alavattam, K.G., Nakata, I.,
669 Weirauch, M.T., Barski, A., and Namekawa, S.H. (2020). Super-enhancer switching drives a
670 burst in gene expression at the mitosis-to-meiosis transition. Nat Struct Mol Biol *27*, 978-988.
671 Manterola, M., Brown, T.M., Oh, M.Y., Garyn, C., Gonzalez, B.J., and Wolgemuth, D.J. (2018).
672 BRDT is an essential epigenetic regulator for proper chromatin organization, silencing of sex
673 chromosomes and crossover formation in male meiosis. PLoS genetics *14*, e1007209.
674 Marcet-Ortega, M., Pacheco, S., Martinez-Marchal, A., Castillo, H., Flores, E., Jasin, M.,
675 Keeney, S., and Roig, I. (2017). p53 and TAp63 participate in the recombination-dependent
676 pachytene arrest in mouse spermatocytes. PLoS genetics *13*, e1006845.
677 Mytlis, A., Kumar, V., Qiu, T., Deis, R., Hart, N., Levy, K., Masek, M., Shawahny, A., Ahmad, A.,
678 Eitan, H.*, et al.* (2022). Control of meiotic chromosomal bouquet and germ cell morphogenesis
679 by the zygotene cilium. Science, eabh3104.
680 Ozata, D.M., Yu, T., Mou, H., Gainetdinov, I., Colpan, C., Cecchini, K., Kaymaz, Y., Wu, P.H.,
681 Fan, K., Kucukural, A.*, et al.* (2020). Evolutionarily conserved pachytene piRNA loci are highly
682 divergent among modern humans. Nat Ecol Evol *4*, 156-168.
683 Papanikos, F., Clement, J.A.J., Testa, E., Ravindranathan, R., Grey, C., Dereli, I., Bondarieva,
684 A., Valerio-Cabrera, S., Stanzione, M., Schleiffer, A.*, et al.* (2019). Mouse ANKRD31
685 Regulates Spatiotemporal Patterning of Meiotic Recombination Initiation and Ensures
686 Recombination between X and Y Sex Chromosomes. Molecular cell *74*, 1069-1085 e1011.

687 Pertea, M., Kim, D., Pertea, G.M., Leek, J.T., and Salzberg, S.L. (2016). Transcript-level
688 expression analysis of RNA-seq experiments with HISAT, StringTie and Ballgown. Nature
689 protocols *11*, 1650-1667.
690 Pertea, M., Pertea, G.M., Antonescu, C.M., Chang, T.C., Mendell, J.T., and Salzberg, S.L.
691 (2015). StringTie enables improved reconstruction of a transcriptome from RNA-seq reads.
692 Nature biotechnology *33*, 290-295.
693 Qiao, H., Prasada Rao, H.B., Yang, Y., Fong, J.H., Cloutier, J.M., Deacon, D.C., Nagel, K.E.,
694 Swartz, R.K., Strong, E., Holloway, J.K.*, et al.* (2014). Antagonistic roles of ubiquitin ligase
695 HEI10 and SUMO ligase RNF212 regulate meiotic recombination. Nature genetics *46*,
696 194-199.
697 Rabbani, M., Zheng, X., Manske, G.L., Vargo, A., Shami, A.N., Li, J.Z., and Hammoud, S.S.
698 (2022). Decoding the Spermatogenesis Program: New Insights from Transcriptomic Analyses.
699 Annu Rev Genet *56*, 339-368.
700 Ramirez, F., Dundar, F., Diehl, S., Gruning, B.A., and Manke, T. (2014). deepTools: a flexible
701 platform for exploring deep-sequencing data. Nucleic acids research *42*, W187-191.
702 Rao, H.B., Qiao, H., Bhatt, S.K., Bailey, L.R., Tran, H.D., Bourne, S.L., Qiu, W., Deshpande, A.,
703 Sharma, A.N., Beebout, C.J.*, et al.* (2017). A SUMO-ubiquitin relay recruits proteasomes to
704 chromosome axes to regulate meiotic recombination. Science *355*, 403-407.
705 Reynolds, A., Qiao, H.Y., Yang, Y., Chen, J.K., Jackson, N., Biswas, K., Holloway, J.K.,
706 Baudat, F., de Massy, B., Wang, J.*, et al.* (2013). RNF212 is a dosage-sensitive regulator of
707 crossing-over during mammalian meiosis. Nature genetics *45*, 269-278.
708 Roeder, G.S., and Bailis, J.M. (2000). The pachytene checkpoint. Trends in genetics : TIG *16*,

709 395-403.

710 Royo, H., Prosser, H., Ruzankina, Y., Mahadevaiah, S.K., Cloutier, J.M., Baumann, M.,
711 Fukuda, T., Hoog, C., Toth, A., de Rooij, D.G., *et al.* (2013). ATR acts stage specifically to
712 regulate multiple aspects of mammalian meiotic silencing. Genes & development *27*,
713 1484-1494.

714 San Filippo, J., Sung, P., and Klein, H. (2008). Mechanism of eukaryotic homologous
715 recombination. Annual review of biochemistry *77*, 229-257.

716 Shibuya, H., Ishiguro, K., and Watanabe, Y. (2014). The TRF1-binding protein TERB1
717 promotes chromosome movement and telomere rigidity in meiosis. Nature cell biology *16*,
718 145-156.

719 Spruce, C., Dlamini, S., Ananda, G., Bronkema, N., Tian, H., Paigen, K., Carter, G.W., and
720 Baker, C.L. (2020). HELLS and PRDM9 form a pioneer complex to open chromatin at meiotic
721 recombination hot spots. Genes & development *34*, 398-412.

722 Subramanian, A., Tamayo, P., Mootha, V.K., Mukherjee, S., Ebert, B.L., Gillette, M.A.,
723 Paulovich, A., Pomeroy, S.L., Golub, T.R., Lander, E.S., *et al.* (2005). Gene set enrichment
724 analysis: a knowledge-based approach for interpreting genome-wide expression profiles.
725 Proceedings of the National Academy of Sciences of the United States of America *102*,
726 15545-15550.

727 Subramanian, V.V., and Hochwagen, A. (2014). The meiotic checkpoint network: step-by-step
728 through meiotic prophase. Cold Spring Harbor perspectives in biology *6*, a016675.

729 Sun, S., Jiang, N., Jiang, Y., He, Q., He, H., Wang, X., Yang, L., Li, R., Liu, F., Lin, X., *et al.*
730 (2020). Chromatin remodeler Znhit1 preserves hematopoietic stem cell quiescence by

731 determining the accessibility of distal enhancers. Leukemia *34*, 3348-3358.

732 Sun, S., Jiang, Y., Zhang, Q., Pan, H., Li, X., Yang, L., Huang, M., Wei, W., Wang, X., Qiu, M.*,*

733 *et al.* (2022). Znhit1 controls meiotic initiation in male germ cells by coordinating with Stra8 to

734 activate meiotic gene expression. Developmental cell *57*, 901-913 e904.

735 Symington, L.S. (2014). End resection at double-strand breaks: mechanism and regulation.

736 Cold Spring Harbor perspectives in biology *6*.

737 Turner, J.M. (2015). Meiotic Silencing in Mammals. Annu Rev Genet *49*, 395-412.

738 Turner, J.M., Mahadevaiah, S.K., Fernandez-Capetillo, O., Nussenzweig, A., Xu, X., Deng,

739 C.X., and Burgoyne, P.S. (2005). Silencing of unsynapsed meiotic chromosomes in the mouse.

740 Nature genetics *37*, 41-47.

741 Wang, L., Xu, Z., Khawar, M.B., Liu, C., and Li, W. (2017). The histone codes for meiosis.

742 Reproduction *154*, R65-R79.

743 Wang, Y., Chen, Y., Chen, J., Wang, L., Nie, L., Long, J., Chang, H., Wu, J., Huang, C., and

744 Lei, M. (2019). The meiotic TERB1-TERB2-MAJIN complex tethers telomeres to the nuclear

745 envelope. Nature communications *10*, 564.

746 Wang, Y., and Copenhaver, G.P. (2018). Meiotic Recombination: Mixing It Up in Plants. Annu

747 Rev Plant Biol *69*, 577-609.

748 Wei, W., Tang, X., Jiang, N., Ni, C., He, H., Sun, S., Yu, M., Yu, C., Qiu, M., Yan, D.*, et al.*

749 (2022). Chromatin remodeler Znhit1 controls bone morphogenetic protein signaling in

750 embryonic lung tissue branching. The Journal of biological chemistry *298*, 102490.

751 Wu, T., Hu, E., Xu, S., Chen, M., Guo, P., Dai, Z., Feng, T., Zhou, L., Tang, W., Zhan, L.*, et al.*

752 (2021). clusterProfiler 4.0: A universal enrichment tool for interpreting omics data. Innovation

753 (Camb) *2*, 100141.

754 Xu, M., Yao, J., Shi, Y., Yi, H., Zhao, W., Lin, X., and Yang, Z. (2021). The SRCAP chromatin
755 remodeling complex promotes oxidative metabolism during prenatal heart development.
756 Development *148*.

757 Xu, Y., Ayrapetov, M.K., Xu, C., Gursoy-Yuzugullu, O., Hu, Y., and Price, B.D. (2012). Histone
758 H2A.Z controls a critical chromatin remodeling step required for DNA double-strand break
759 repair. Molecular cell *48*, 723-733.

760 Yamada, S., Kugou, K., Ding, D.Q., Fujita, Y., Hiraoka, Y., Murakami, H., Ohta, K., and
761 Yamada, T. (2018). The histone variant H2A.Z promotes initiation of meiotic recombination in
762 fission yeast. Nucleic acids research *46*, 609-620.

763 Yoshida, S., Sukeno, M., Nakagawa, T., Ohbo, K., Nagamatsu, G., Suda, T., and Nabeshima,
764 Y. (2006). The first round of mouse spermatogenesis is a distinctive program that lacks the
765 self-renewing spermatogonia stage. Development *133*, 1495-1505.

766 Yoshida, S., Takakura, A., Ohbo, K., Abe, K., Wakabayashi, J., Yamamoto, M., Suda, T., and
767 Nabeshima, Y. (2004). Neurogenin3 delineates the earliest stages of spermatogenesis in the
768 mouse testis. Developmental biology *269*, 447-458.

769 Yu, J., Sui, F., Gu, F., Li, W., Yu, Z., Wang, Q., He, S., Wang, L., and Xu, Y. (2024). Structural
770 insights into histone exchange by human SRCAP complex. Cell Discov *10*, 15.

771 Yu, T., Fan, K., Ozata, D.M., Zhang, G., Fu, Y., Theurkauf, W.E., Zamore, P.D., and Weng, Z.
772 (2021). Long first exons and epigenetic marks distinguish conserved pachytene piRNA
773 clusters from other mammalian genes. Nature communications *12*, 73.

774 Zhang, Q., Ji, S.Y., Busayavalasa, K., and Yu, C. (2019). SPO16 binds SHOC1 to promote

775 homologous recombination and crossing-over in meiotic prophase I. Sci Adv *5*, eaau9780.

776 Zhang, Y., Liu, T., Meyer, C.A., Eeckhoute, J., Johnson, D.S., Bernstein, B.E., Nusbaum, C.,

777 Myers, R.M., Brown, M., Li, W.*, et al.* (2008). Model-based analysis of ChIP-Seq (MACS).

778 Genome biology *9*, R137.

779 Zhao, B., Chen, Y., Jiang, N., Yang, L., Sun, S., Zhang, Y., Wen, Z., Ray, L., Liu, H., Hou, G.*,*

780 *et al.* (2019). Znhit1 controls intestinal stem cell maintenance by regulating H2A.Z

781 incorporation. Nature communications *10*, 1071.

782 Zheng, H., and Xie, W. (2019). The role of 3D genome organization in development and cell

783 differentiation. Nature reviews Molecular cell biology.

784 Zickler, D., and Kleckner, N. (2023). Meiosis: Dances Between Homologs. Annu Rev Genet.

785

786

Acknowledgments: We thank Chuan He for N3-kethoxal and Christopher L. Baker for meiotic chromatin state data. **Funding:** This work was supported by grants from the National Key Research and Development Program of China (2022YFA0806200, 2018YFC1003500, 2018YFA0800100, 2021YFC2501800), the National Natural Science Foundation of China (32192400, 81971443, 32300702, 32350710191), the Science and Technology Major Project of Inner Mongolia Autonomous Region of China to the State Key Laboratory of Reproductive Regulation and Breeding of Grassland Livestock (2020ZD0008). Shenfei Sun was supported by the fellowship of China Postdoctoral Science Foundation (2022M720797) and the Postdoctoral Fellowship Program (Grade B) of China Postdoctoral Science Foundation (GZB20230161).

Author Contributions: S.S. and X.L. conceived and designed the study; S.S. performed most of the experiments with the help of Y.J., Q.Z., H.P., F.H., X.Z., Y.G., X.Y., K.G., W.W., H.L., Z.S., Y.S., X.T., M.Y., and R.L.; Y.J. and N.J. performed the bioinformatics analysis; X.L. supervised the work and acquired the funding support; and S.S. and X.L. wrote the manuscript, with contributions from all authors. **Competing interests:** The authors declare that they have no competing interests. **Data and materials availability:** The NGS data generated in this study were deposited in the NCBI SRA database under accession numbers SRP467214 (RNA-seq and ChIP-seq data) and SRP467448 (ATAC-seq and KAS-seq data).

Figure 1 | *Znhit1* deletion in spermatocytes disrupts spermatogenesis. (**A**) Schematic representation of the male germline development in mice. (**B**) Heatmap showing the clustering of 47 chromatin factors based on the transcription levels in leptotene and zygotene spermatocytes. (**C**) *Znhit1* in situ hybridization in postnatal day 60 (P60) testis sections. Scale bar, 20 μm. Sg, spermatogonia; pL, preleptotene; L, leptotene; Z, zygotene; P, pachytene; D, diplotene; MI, metaphase; R, round spermatids; E, elongating spermatids. (**D**) Schematic diagram showing the onset of Stra8-cre expression in the male germline development. (**E**) *Znhit1* in situ hybridization in P42 testis sections. Scale bar, 50 μm. (**F**) Histological testicular sections in control or *Znhit1*-sKO testis sections at the indicated times. Scale bar, 50 μm. (**G**) Immunostaining of PNA in testis sections from control or *Znhit1*-sKO mice at the indicated times. rST, round spermatids; eST, elongating spermatids. Scale bar, 20 μm. All images are representative of n = 3 mice per genotype.

Figure 2 | *Znhit1* deletion leads to meiotic pachytene arrest. (**A**-**C**) Immunostaining of SYCP3 in spermatocyte chromosome spreads of control (**A**) or *Znhit1*-sKO mice (**B**). Quantitative data are shown in (**C**). Scale bar, 10 μm. (**D** and **E**) TUNEL staining in testis sections from P14 control or *Znhit1*-sKO mice. Quantitative data are shown in (**E**). Scale bar, 40 μm. All images are representative of n = 3 mice per genotype. (**F**) UMAP plot showing the annotated cells captured from P35 control and *Znhit1*-sKO testicular cells. (**G**) UMAP plot showing the expression of *Znhit1* and *Pou5f2* in control P35 control and *Znhit1*-sKO testicular cells. Data are presented as the mean ± s.d. *** $p < 0.001$.

Figure 3 | *Znhit1* deletion impairs meiotic recombination. (**A** and **B**) Immunostaining of SYCP3 and SYCP1 in spermatocyte chromosome spreads of control or *Znhit1*-sKO mice. Arrows indicate autosomal regions with abnormal synapsis. X, X chromosome; Y, Y chromosome; PAR, pseudoautosomal region. Quantitative data are shown in (**B**). Scale bar, 10 μm. (**C**) Immunostaining of SYCP3 and γH2AX in spermatocyte chromosome

spreads of control or *Znhit1*-sKO mice. Scale bar, 10 μm. (**D** and **E**) Immunostaining of SYCP3 and RAD51 in spermatocyte chromosome spreads of control or *Znhit1*-sKO mice. Quantitative data are shown in (**E**). Scale bar, 10 μm. (**F**) Immunostaining of SYCP3 and MLH1 in spermatocyte chromosome spreads of control or *Znhit1*-sKO mice. Scale bar, 10 μm. All images are representative of n = 3 mice per genotype. Data are presented as the mean ± s.d. *** $p < 0.001$.

Figure 4 | *Znhit1* deletion impairs meiotic transcriptional programs. (**A**) UMAP plot showing the annotated cells captured from P16 control and *Znhit1*-sKO testicular cells. (**B**) Violin plots showing the average expression level of upregulated or downregulated genes between two consecutive spermatocyte stages. PreL, preleptotene; Lep, leptotene; Zyg, zygotene; Pac, pachytene. (**C**) Volcano plot showing the distribution of upregulated and downregulated DEGs for each cell type in spermatocytes between control and *Znhit1*-sKO testicular cells. (**D** and **E**) Representative shared Gene Ontology (GO) terms of upregulated and downregulated DEGs at consecutive spermatocyte stages. (**F**) Volcano plot showing differentially expressed XY-linked genes in scRNA-seq data following *Znhit1* deletion.

Figure 5 | ZNHIT1 regulates H2A.Z binding on promoter and enhancer regions. (**A**) Immunostaining of SYCP3 and H2A.Z in spermatocyte chromosome spreads of control or *Znhit1*-sKO mice. The dashed circle indicates X-Y chromosomes. Scale bar, 10 μm. (**B**) Representative tracks of END-seq, DMC1-SSDS, and H2A.Z ChIP-seq in wild-type, control, or *Znhit1*-sKO testicular cells. (**C**) Heatmaps of chromatin states produced by ChromHMM and showing different enrichment for H2A.Z in control or *Znhit1*-sKO testicular cells. (**D**) Heatmaps and mean plots of H2A.Z ChIP-seq signal in control or *Znhit1*-sKO testicular cells (n = 2). (**E**) Venn diagram showing the overlap between decreased H2A.Z-bound genes and downregulated genes in *Znhit1*-sKO testicular cells.

(**F**) Heatmaps and mean plots of downregulated H2A.Z ChIP-seq signals surrounding different types of promoters and enhancers.

Figure 6 | ZNHIT1/H2A.Z/A-MYB axis regulates chromatin state and gene expression. (**A**) Motif analysis of active promoters or active enhancers with decreased H2A.Z binding for putative transcription factor (TF)-binding sites using the HOMER database. (**B**) Ridge map showing the A-MYB activity (AUC) at each cell type. (**C**) Scatter plot with marginal histograms comparing the fold change of DEGs from *Mybl1*-related RNA-seq data with *Znhit1*-related RNA-seq data in P14 testicular cells. (**D**) GSEA of RNA-seq data for the control and *Znhit1*-sKO testicular cells. Selected gene sets encoded products related to A-MYB target genes. (**E**) Violin plots showing the expression of A-MYB target genes at consecutive spermatocyte stages. (**F**) Histogram showing H2A.Z and A-MYB binding sites. (**G**) Pie chart showing the distribution of H2A.Z and A-MYB co-binding sites. (**H**) Representative H2A.Z ChIP-seq tracks, KAS-seq signals, and RNA-seq signals of the *Ccnb1ip1* locus in the control and *Znhit1*-sKO testicular cells, compared with A-MYB ChIP-seq peaks. (**I**) Heatmaps and mean plots of H2A.Z ChIP-seq, KAS-seq, and ATAC-seq showing signal changes within A-MYB and H2A.Z co-binding active promoters or active enhancers. ******** $p < 0.0001$.

Figure 1

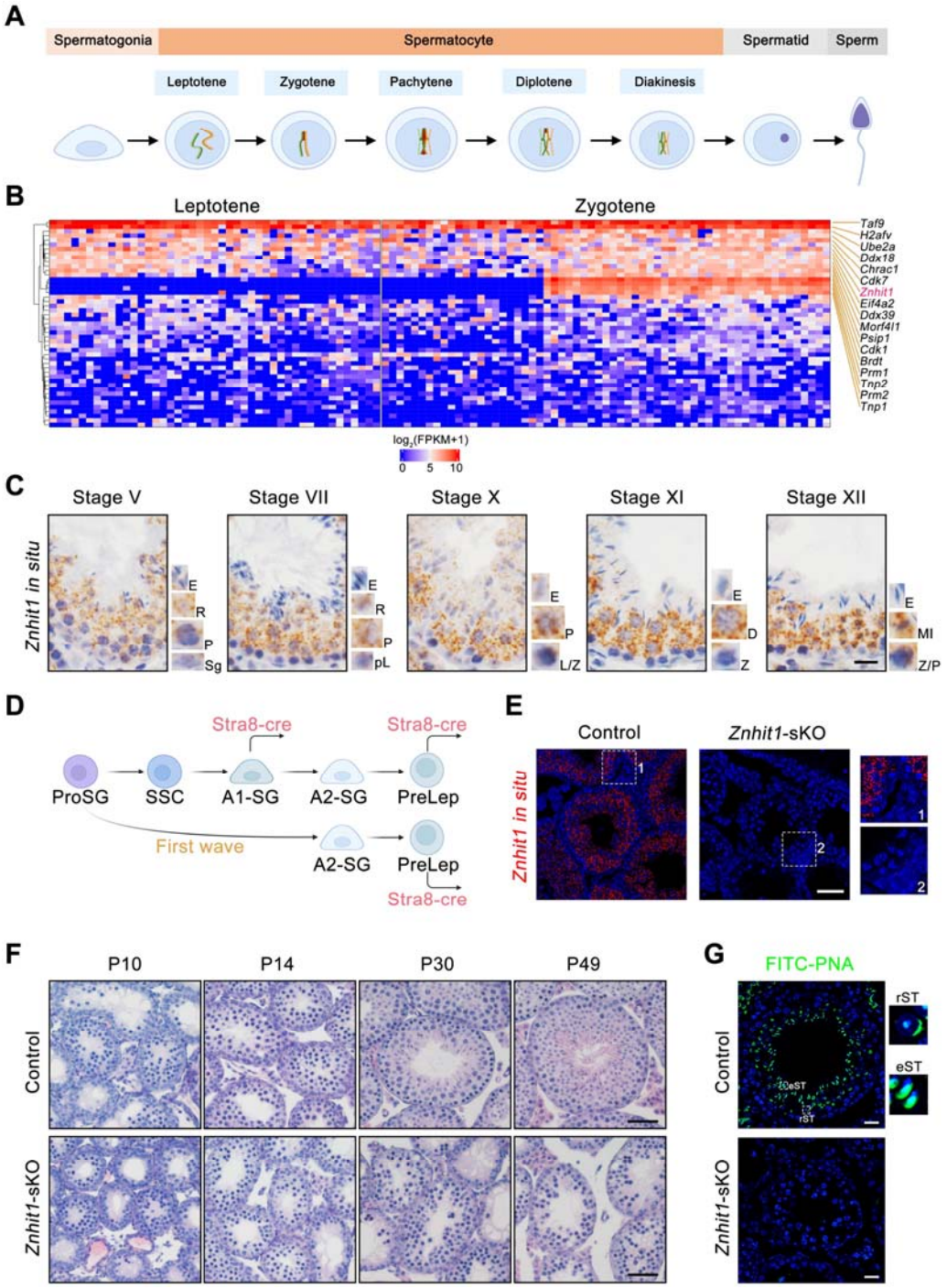
A
Spermatogonia
Spermatocyte
Spermatid
Sperm
Leptotene
Zygotene
Pachytene
Diplotene
Diakinesis
B
Leptotene
Zygotene
Taf9
H2afv
Ube2a
Ddx18
Chrac1
Cdk7
Znhit1
Eif4a2
Ddx39
Morf4l1
Psip1
Cdk1
Brdt
Prm1
Tnp2
Prm2
Tnp1
log2(FPKM+1)
0 5 10
C
Stage V
Stage VII
Stage X
Stage XI
Stage XII
Znhit1 in situ
E
R
P
Sg
pL
L/Z
D
Z
MI
Z/P
D
Stra8-cre
ProSG
SSC
A1-SG
A2-SG
PreLep
First wave
E
Control
Znhit1-sKO
Znhit1 in situ
1
2
F
P10
P14
P30
P49
Control
Znhit1-sKO
G
FITC-PNA
rST
eST
Control
Znhit1-sKO

Figure 2

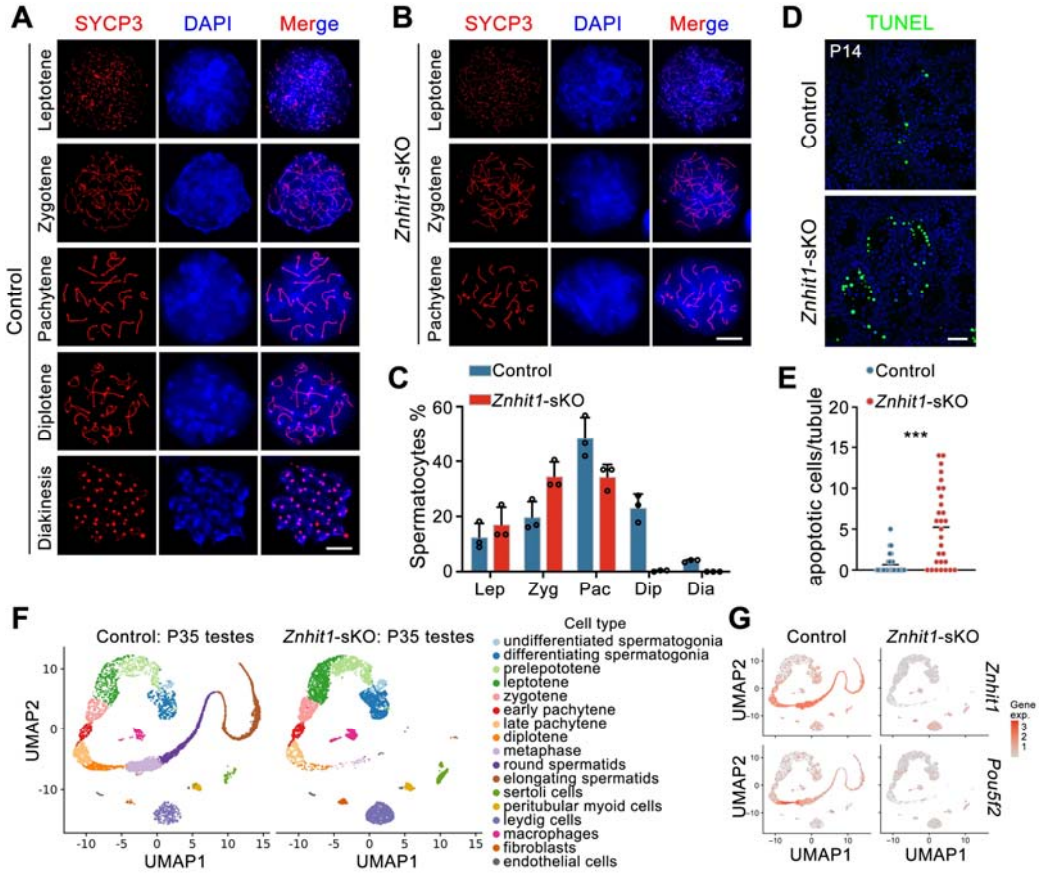
A
SYCP3
DAPI
Merge
Control
Leptotene
Zygotene
Pachytene
Diplotene
Diakinesis
B
SYCP3
DAPI
Merge
Znhit1-sKO
Leptotene
Zygotene
Pachytene
D
TUNEL
P14
Control
Znhit1-sKO
C
Control
Znhit1-sKO
Spermatocytes %
Lep
Zyg
Pac
Dip
Dia
E
Control
Znhit1-sKO
apoptotic cells/tubule
***
F
Control: P35 testes
Znhit1-sKO: P35 testes
UMAP2
UMAP1
Cell type
undifferentiated spermatogonia
differentiating spermatogonia
prelepototene
leptotene
zygotene
early pachytene
late pachytene
diplotene
metaphase
round spermatids
elongating spermatids
sertoli cells
peritubular myoid cells
leydig cells
macrophages
fibroblasts
endothelial cells
G
Control
Znhit1-sKO
Znhit1
Pou5f2
Gene exp.

Figure 3

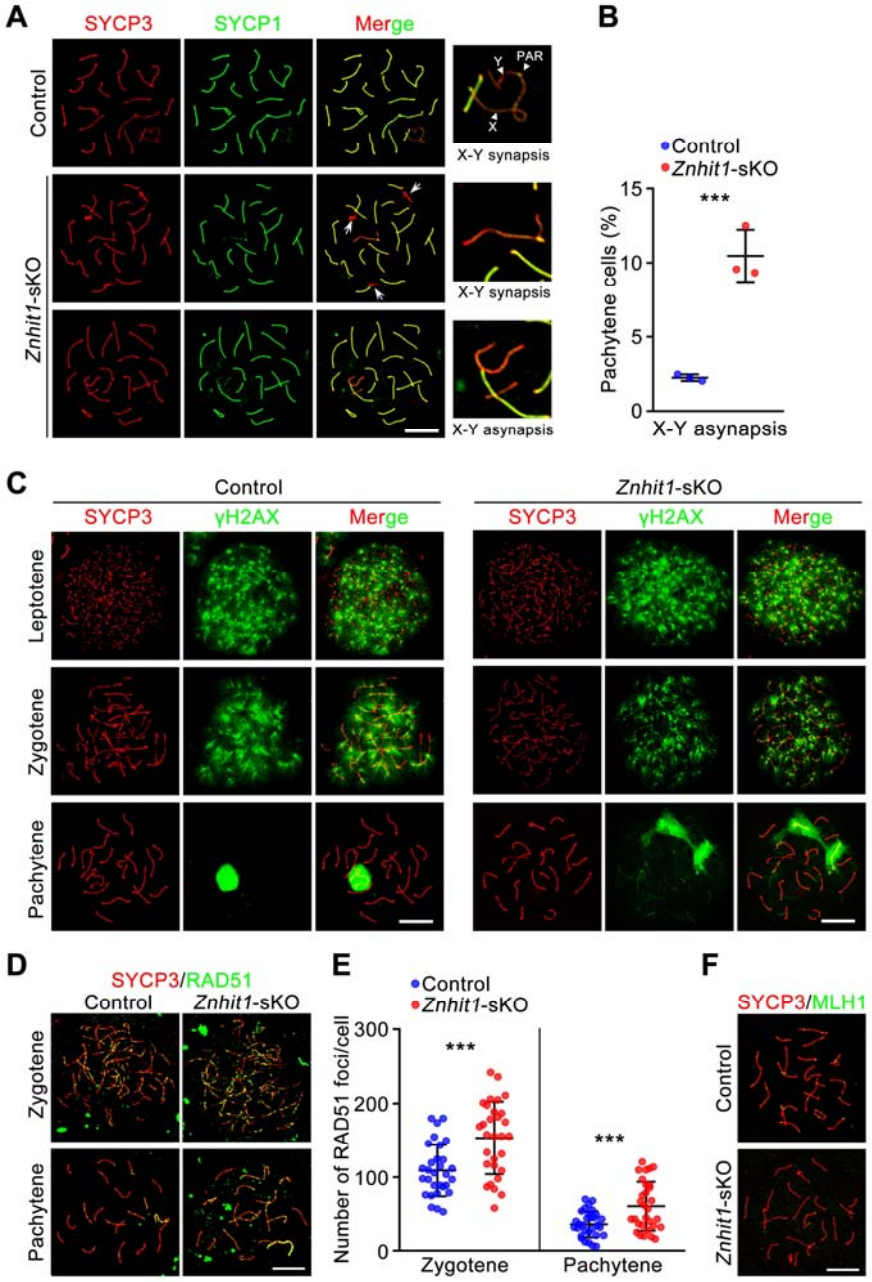
A
SYCP3
SYCP1
Merge
Control
Znhit1-sKO
Y
PAR
X
X-Y synapsis
X-Y synapsis
X-Y asynapsis
B
Control
Znhit1-sKO
***
Pachytene cells (%)
15
10
5
0
X-Y asynapsis
C
Control
Znhit1-sKO
SYCP3
γH2AX
Merge
Leptotene
Zygotene
Pachytene
D
SYCP3/RAD51
Control
Znhit1-sKO
Zygotene
Pachytene
E
Control
Znhit1-sKO
Number of RAD51 foci/cell
300
200
100
0
***
***
Zygotene
Pachytene
F
SYCP3/MLH1
Control
Znhit1-sKO

Figure 4

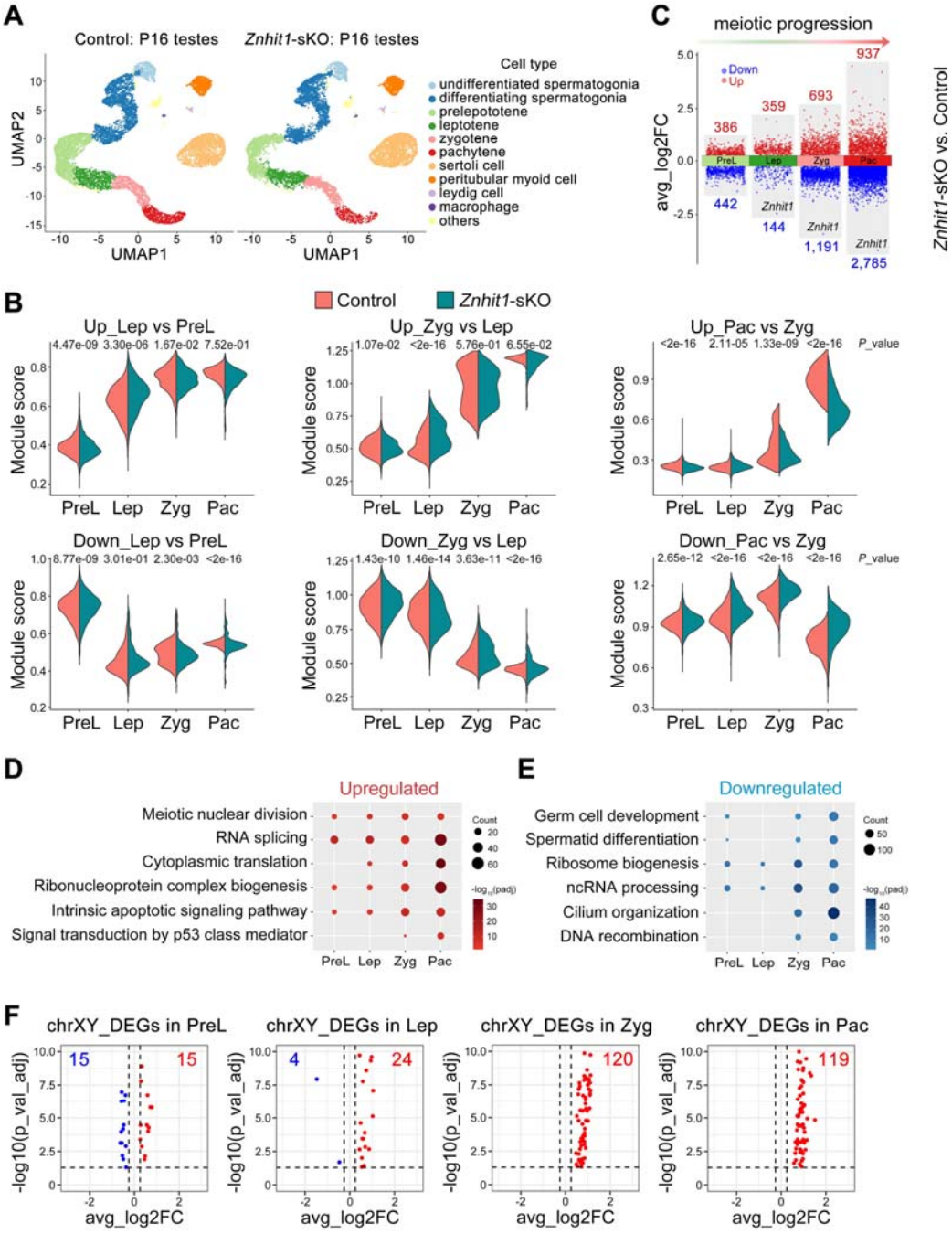
A
Control: P16 testes
Znhit1-sKO: P16 testes
UMAP2
UMAP1
Cell type
undifferentiated spermatogonia
differentiating spermatogonia
prelepototene
leptotene
zygotene
pachytene
sertoli cell
peritubular myoid cell
leydig cell
macrophage
others
C
meiotic progression
Down
Up
avg_log2FC
PreL
Lep
Zyg
Pac
386
359
693
937
442
144
1,191
2,785
Znhit1
Znhit1-sKO vs. Control
B
Control
Znhit1-sKO
Up_Lep vs PreL
4.47e-09 3.30e-06 1.67e-02 7.52e-01
Up_Zyg vs Lep
1.07e-02 <2e-16 5.76e-01 6.55e-02
Up_Pac vs Zyg
<2e-16 2.11-05 1.33e-09 <2e-16
P_value
Down_Lep vs PreL
8.77e-09 3.01e-01 2.30e-03 <2e-16
Down_Zyg vs Lep
1.43e-10 1.46e-14 3.63e-11 <2e-16
Down_Pac vs Zyg
2.65e-12 <2e-16 <2e-16 <2e-16
Module score
D
Upregulated
Meiotic nuclear division
RNA splicing
Cytoplasmic translation
Ribonucleoprotein complex biogenesis
Intrinsic apoptotic signaling pathway
Signal transduction by p53 class mediator
Count
E
Downregulated
Germ cell development
Spermatid differentiation
Ribosome biogenesis
ncRNA processing
Cilium organization
DNA recombination
F
chrXY_DEGs in PreL
chrXY_DEGs in Lep
chrXY_DEGs in Zyg
chrXY_DEGs in Pac
15
15
4
24
120
119
-log10(p_val_adj)
avg_log2FC

Figure 5

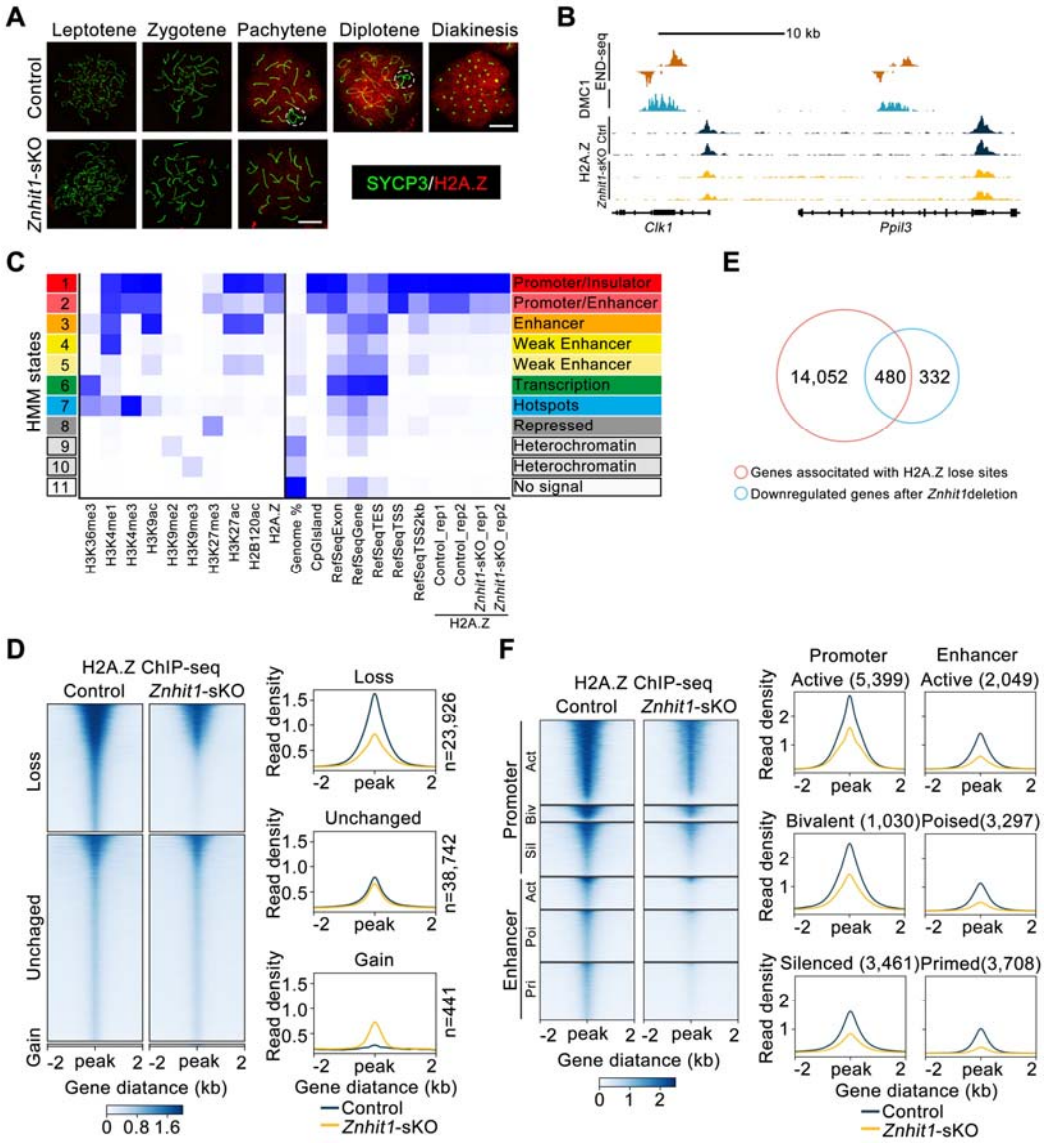
A
Leptotene
Zygotene
Pachytene
Diplotene
Diakinesis
Control
Znhit1-sKO
SYCP3/H2A.Z
B
10 kb
DMC1
END-seq
H2A.Z
Znhit1-sKO
Ctrl
Clk1
Ppil3
C
HMM states
Promoter/Insulator
Promoter/Enhancer
Enhancer
Weak Enhancer
Weak Enhancer
Transcription
Hotspots
Repressed
Heterochromatin
Heterochromatin
No signal
H3K36me3
H3K4me1
H3K4me3
H3K9ac
H3K9me2
H3K9me3
H3K27me3
H3K27ac
H2B120ac
H2A.Z
Genome %
CpGIsland
RefSeqExon
RefSeqGene
RefSeqTES
RefSeqTSS
RefSeqTSS2kb
Control_rep1
Control_rep2
Znhit1-sKO_rep1
Znhit1-sKO_rep2
E
14,052
480
332
Genes associated with H2A.Z lose sites
Downregulated genes after Znhit1deletion
D
H2A.Z ChIP-seq
Control
Znhit1-sKO
Loss
Unchaged
Gain
Gene diatance (kb)
Read density
n=23,926
n=38,742
n=441
Control
Znhit1-sKO
F
Promoter
Enhancer
Act
Biv
Sil
Act
Poi
Pri
Promoter Active (5,399)
Enhancer Active (2,049)
Bivalent (1,030)
Poised(3,297)
Silenced (3,461)
Primed(3,708)

Figure 6

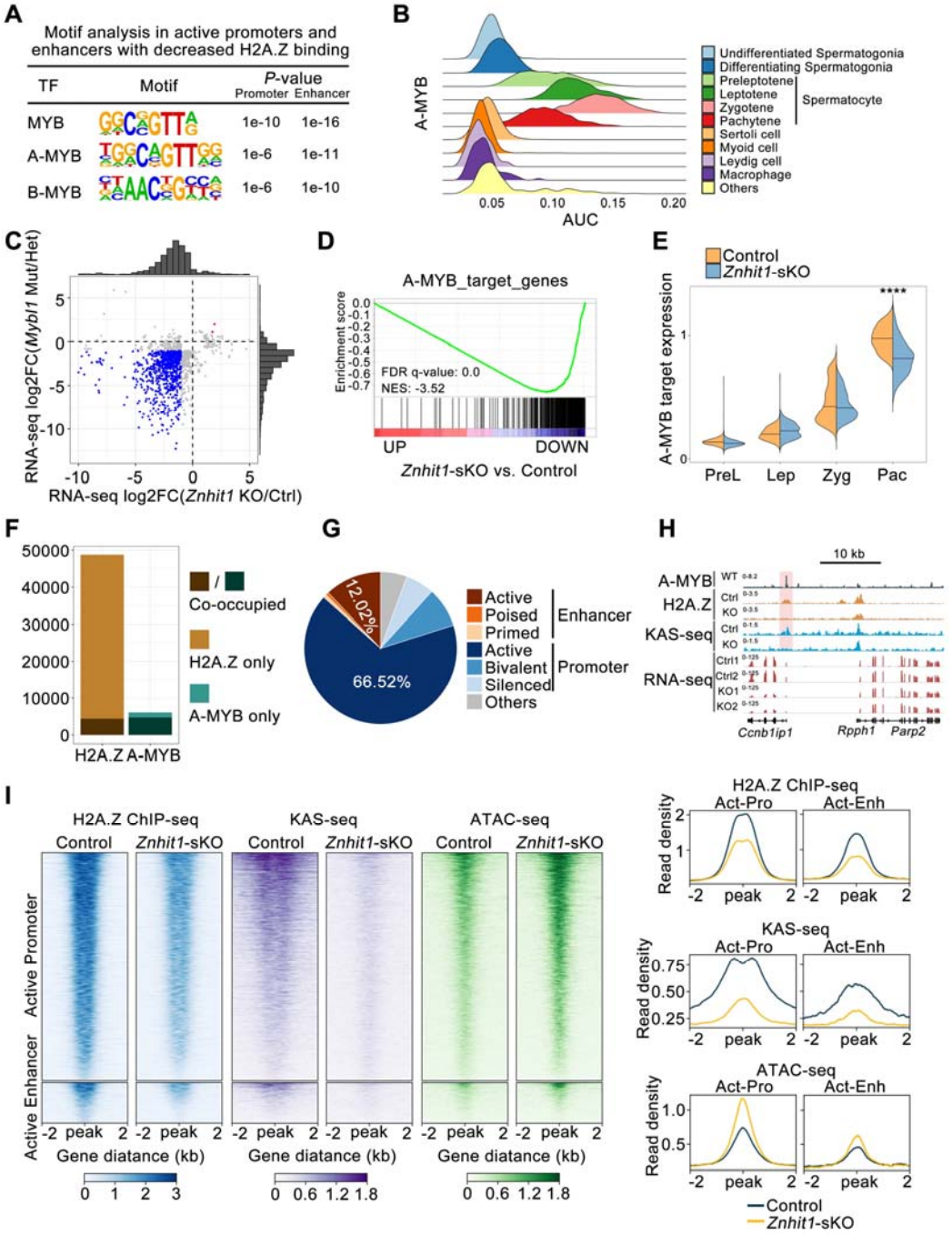
A
Motif analysis in active promoters and enhancers with decreased H2A.Z binding
TF
Motif
P-value
Promoter Enhancer
MYB 1e-10 1e-16
A-MYB 1e-6 1e-11
B-MYB 1e-6 1e-10
B
A-MYB
AUC
Undifferentiated Spermatogonia
Differentiating Spermatogonia
Preleptotene
Leptotene
Zygotene
Pachytene
Spermatocyte
Sertoli cell
Myoid cell
Leydig cell
Macrophage
Others
C
RNA-seq log2FC(Mybl1 Mut/Het)
RNA-seq log2FC(Znhit1 KO/Ctrl)
D
A-MYB_target_genes
Enrichment score
FDR q-value: 0.0
NES: -3.52
UP
DOWN
Znhit1-sKO vs. Control
E
Control
Znhit1-sKO
A-MYB target expression
PreL
Lep
Zyg
Pac
F
Co-occupied
H2A.Z only
A-MYB only
H2A.Z A-MYB
G
12.02%
66.52%
Active
Poised
Primed
Enhancer
Active
Bivalent
Silenced
Promoter
Others
H
10 kb
A-MYB
H2A.Z
KAS-seq
RNA-seq
Ccnb1ip1
Rpph1
Parp2
I
H2A.Z ChIP-seq
KAS-seq
ATAC-seq
Control
Znhit1-sKO
Active Promoter
Active Enhancer
Gene diatance (kb)
Act-Pro
Act-Enh
Read density
peak
Control
Znhit1-sKO

Supplementary Materials for

ZNHIT1-dependent H2A.Z deposition at meiotic prophase I underlies pachytene gene expression and meiotic progression during male meiosis

Shenfei Sun *et al.*

*Corresponding author. Email: Xinhua Lin, xlin@fudan.edu.cn; Shenfei Sun shenfei_sun@fudan.edu.cn

This PDF file includes:

Figs. S1 to S9

Other Supplementary Material for this manuscript includes the following:

Tables. S1 to S8

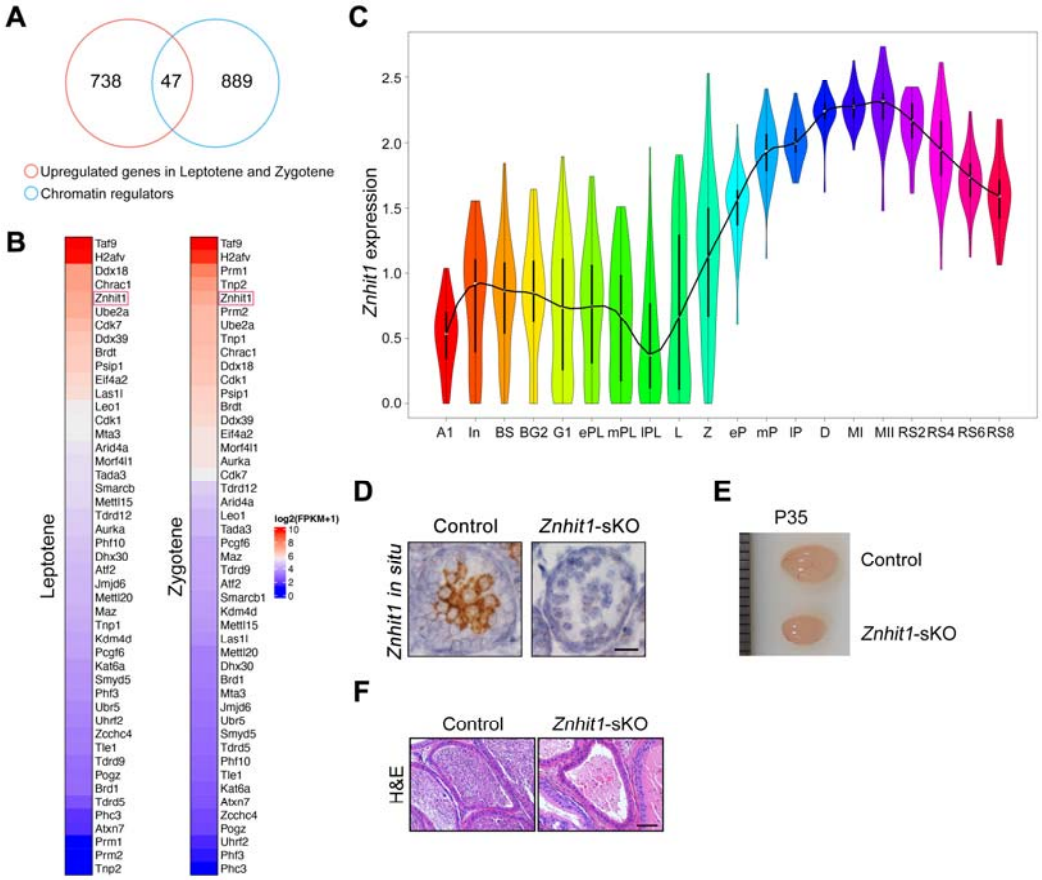

Figure S1. *Znhit1* expression during meiotic progression and spermatocyte-conditional deletion of *Znhit1* with Stra8-cre. (**A** and **B**) Venn diagram and heatmaps showing chromatin regulators highly expressed during leptotene and zygotene spermatocytes. (**C**) Violin plot showing *Znhit1* transcription level during spermatogenesis. Gene expression profiles derived from published scRNA-seq data (Chen et al, 2018). (**D**) *Znhit1* in situ hybridization in P14 testis sections. Scale bar, 20 μm. (**E**) Testis size comparison between control and *Znhit1*-sKO mice at P35. (**F**) Hematoxylin and eosin (H&E) - stained testis sections from control and *Znhit1*-sKO mice at P60. Scale bar, 50 μm.

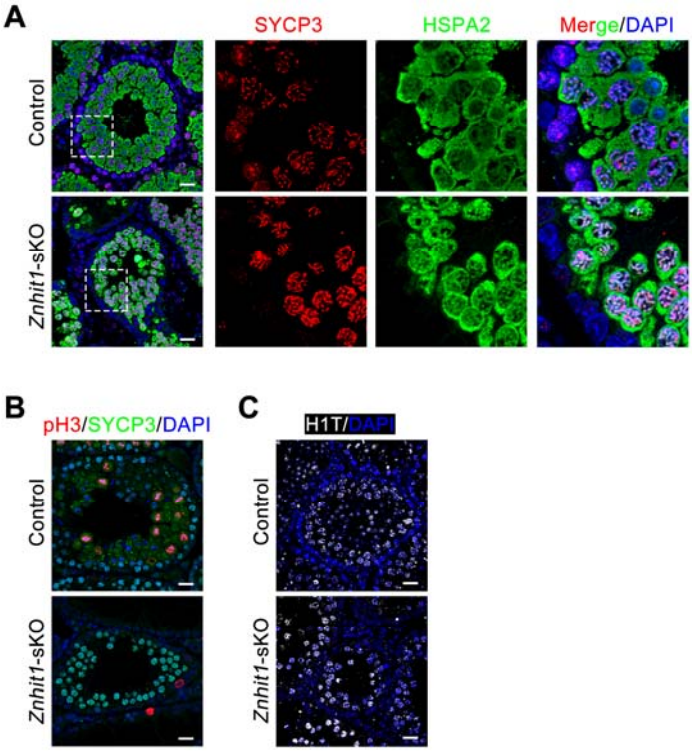

Figure S2. Spermatocyte development in *Znhit1*-sKO testes. (**A**) Immunostaining of SYCP3 and HSPA2 in testis sections of control or *Znhit1*-sKO mice at P35. Scale bar, 20 μm. (**B**) Immunostaining of SYCP3 and pH3 in testis sections of control or *Znhit1*-sKO mice at P35. Scale bar, 20 μm. (**C**) Immunostaining of H1T in testis sections from control and *Znhit1*-sKO mice at P35. Scale bar, 20 μm.

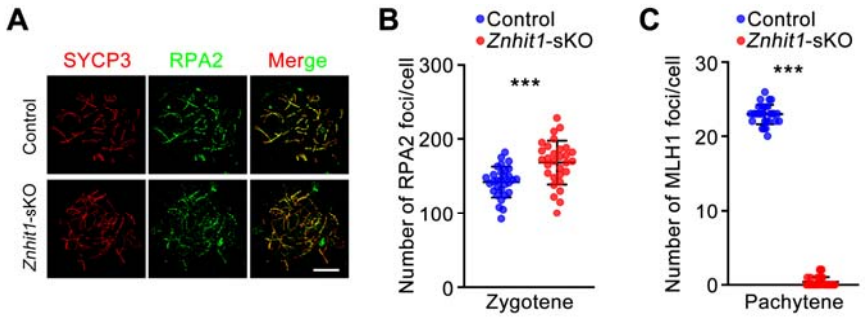

Figure S3. ZNHIT1 is required for meiotic recombination. (**A** and **B**) Immunostaining of SYCP3 and RPA2 in spermatocyte chromosome spreads of control or *Znhit1*-sKO mice. Quantitative data are shown in (**B**). Scale bar, 10 μm. (**C**) Plots showing quantitative data of MLH1 foci of control or *Znhit1*-sKO mice. Data are presented as the mean ± s.d. *** $p < 0.001$

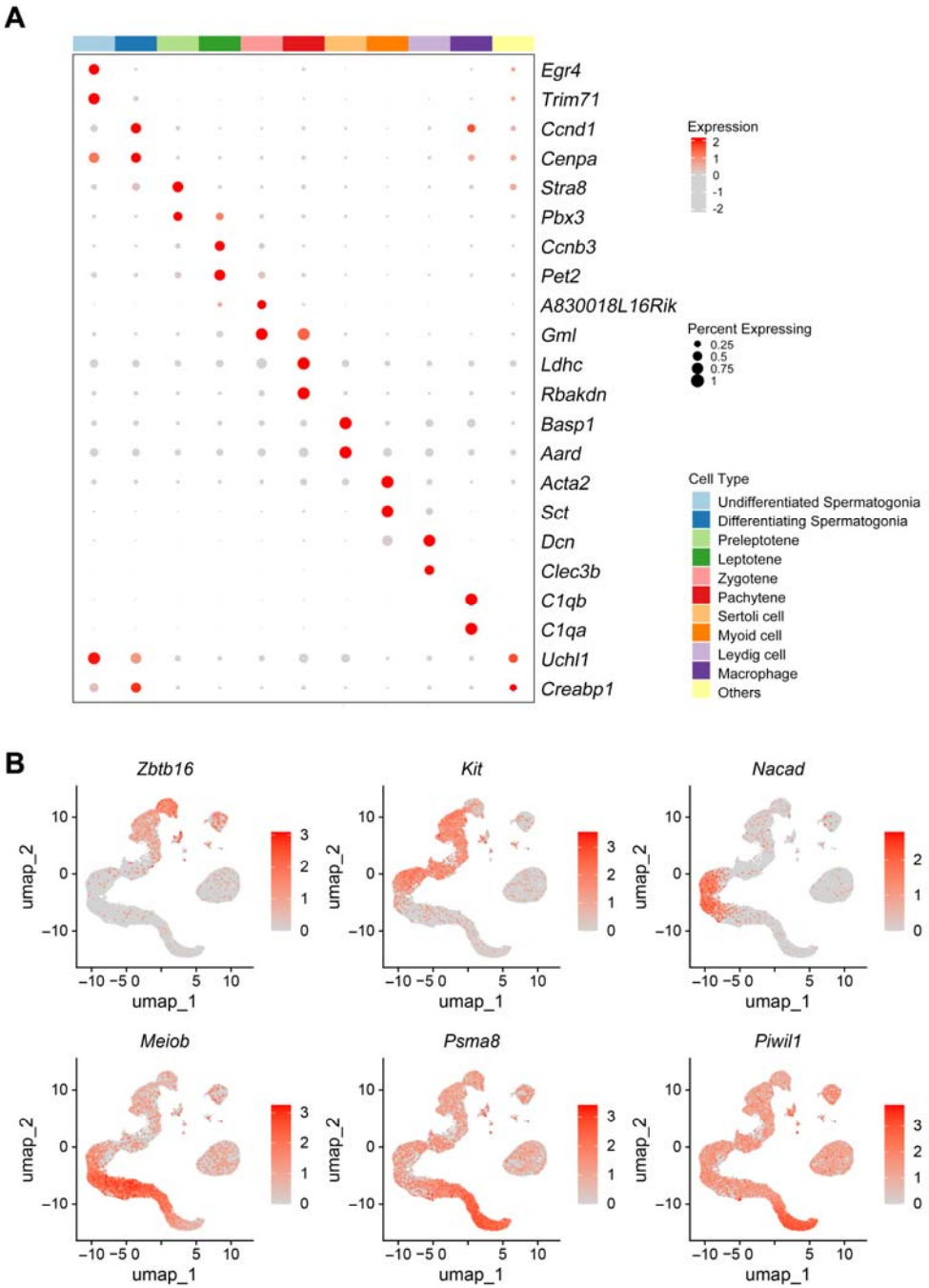

Figure S4. Single-cell RNA-seq of testicular cells. (**A**) Dot plot showing the relative expression and the percentage of cells expressing selected markers across scRNA-seq clusters. (**B**) UMAP plots showing the normalized expression of the indicated genes in scRNA-seq data.

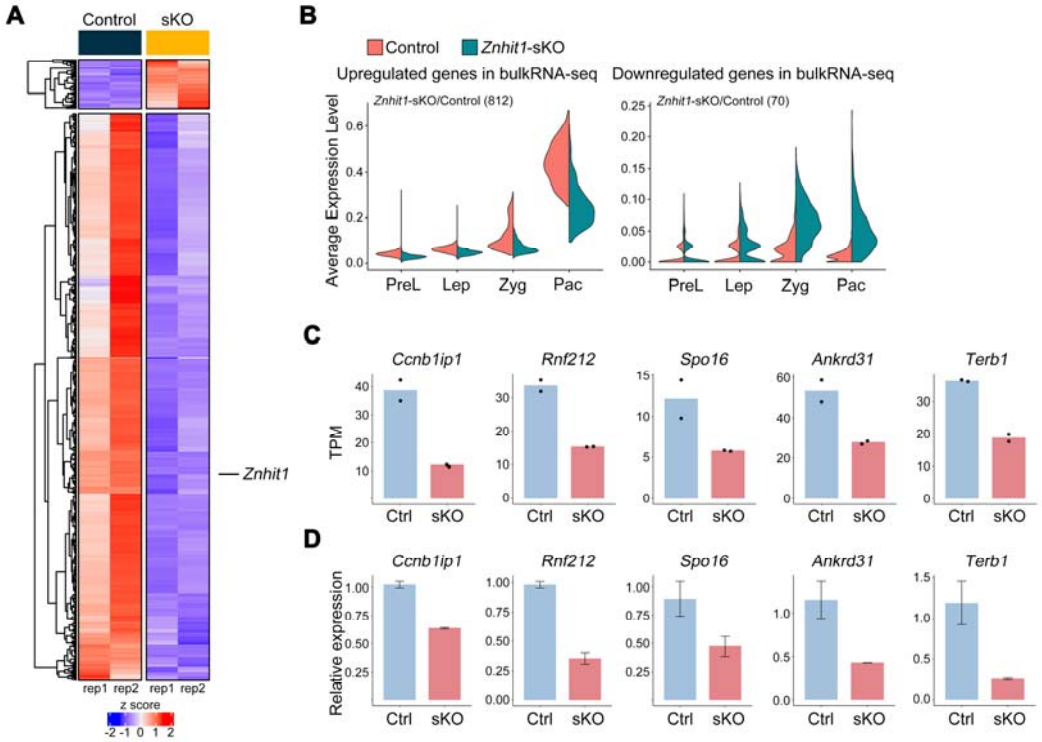

Figure S5. Transcriptomic analysis of testicular cells. (**A**) Heatmap showing differentially expressed genes (DEGs) in P14 testicular cells between control and *Znhit1*-sKO mice. (**B**) Violin plots showing the average expression level of upregulated or downregulated genes between P14 control and *Znhit*1-sKO testicular cells. PreL, preleptotene; Lep, leptotene; Zyg, zygotene; Pac, pachytene. (**C** and **D**) Bar charts showing HR-related gene expression in P14 control and *Znhit*1-sKO testes. Data from bulk RNA-seq are shown in (**C**). Validated data from RT-qPCR are shown in (**D**). Ctrl, control; sKO, *Znhit1*-sKO.

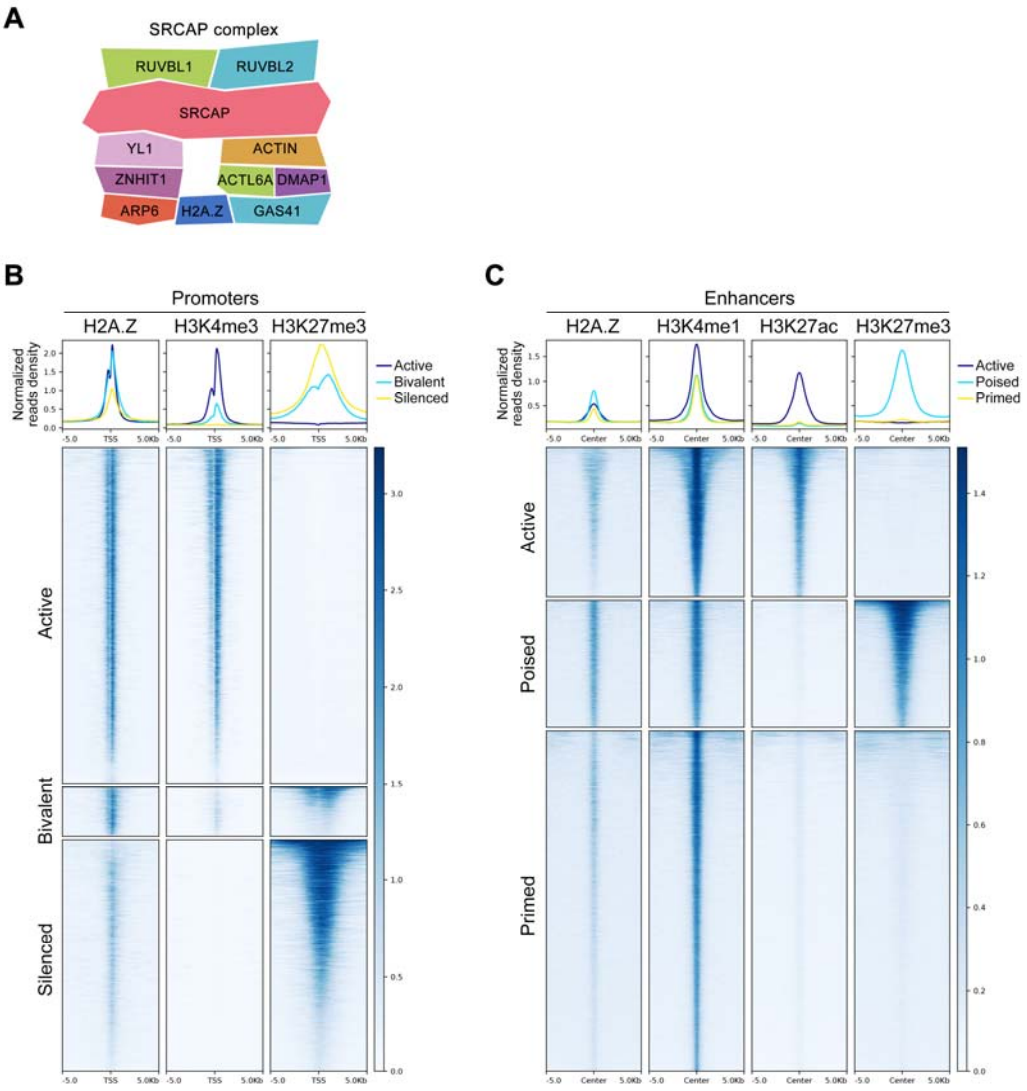

Figure S6. H2A.Z is enriched at meiotic gene promoters and enhancers. (**A**) Schematic representation of the components of the SRCAP chromatin remodeling complex. (**B**) Heatmaps showing H2A.Z ChIP-seq signals surrounding different types of promoters. (**C**) Heatmaps showing H2A.Z ChIP-seq signals surrounding different types of enhancers.

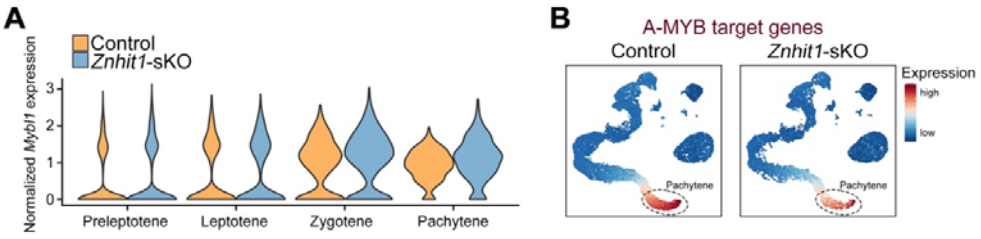

Figure S7. *Znhit1* deletion downregulates the expression of A-MYB target genes. (**A**) Violin plot showing the normalized expression of *Mybl1* in control and *Znhit1*-sKO spermatocytes at consecutive stages. (**B**) Cluster annotation on the basis of the expression of A-MYB target genes in control or *Znhit1*-sKO testicular cells.

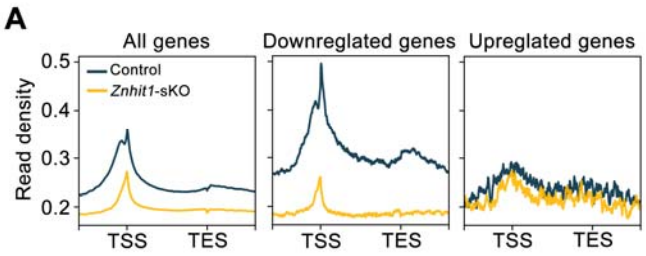

Figure S8. KAS-seq analysis. (**A**) Mean plots of KAS-seq showing signal changes within indicated genes.

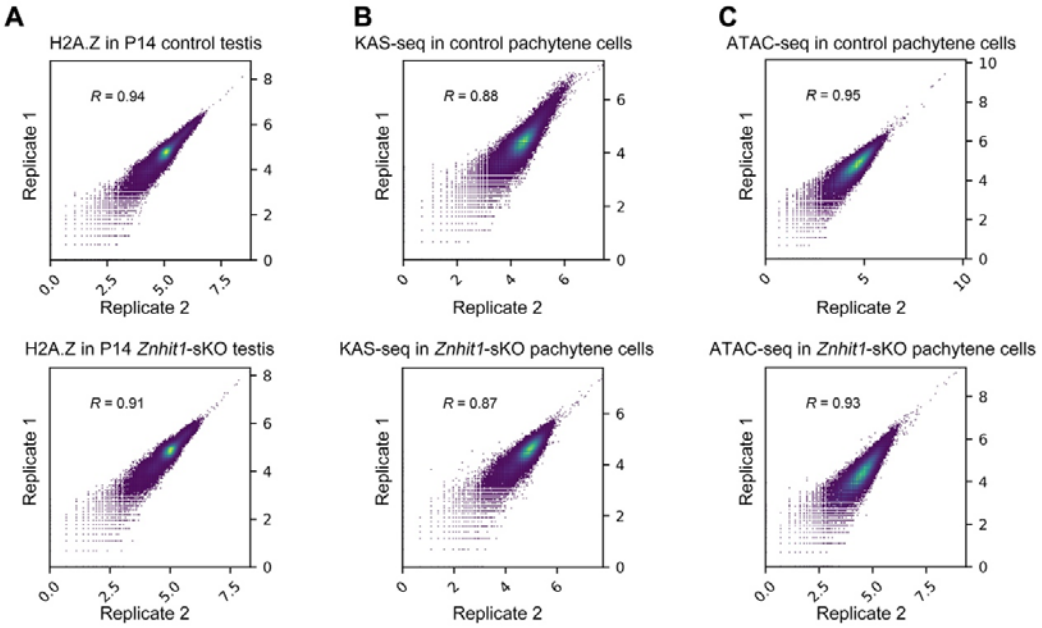

Figure S9. Reproducibility of replicates in this study. (**A**) Scatter plots showing H2A.Z enrichments in P14 control or *Znhit1*-sKO testes for two independent H2A.Z ChIP-seq replicates. Pearson correlation coefficients are indicated. (**B**) Scatter plots showing KAS-seq signals in P14 control or *Znhit1*-sKO pachytene cells for two independent H2A.Z ChIP-seq replicates. Pearson correlation coefficients are indicated. (**C**) Scatter plots showing ATAC-seq signals in P14 control or *Znhit1*-sKO pachytene cells for two independent H2A.Z ChIP-seq replicates. Pearson correlation coefficients are indicated.